Two distinct mechanisms underlie dosage sensitivity in Pumilio1-associated diseases

Salvatore Botta[1,2], Nicola de Prisco[1], Alexei Chemiakine[1], Maximilian Cabaj[1], Vicky L. Brandt[1], Purvi Patel[3], Rajesh K. Soni[3], and Vincenzo A. Gennarino[1,4,5,6,7]

[1]Department of Genetics and Development, Columbia University Irving Medical Center, New York, NY.
[2]Department of Translational Medical Science, University of Campania Luigi Vanvitelli, Caserta, Italy.
[3]Proteomics and Macromolecular Crystallography Shared Resource, Herbert Irving Comprehensive Cancer Center, Columbia University Irving Medical Center, New York, NY.
[4]Departments of Pediatrics and Neurology, Columbia University Irving Medical Center, New York, NY.
[5]Columbia Stem Cell Initiative, Columbia University Irving Medical Center, New York, NY.
[6]Initiative for Columbia Ataxia and Tremor, Columbia University Irving Medical Center, New York, NY.
[7]Corresponding author: vag2138@cumc.columbia.edu

Keywords

Pumilio1 interactome, RNA-binding proteins, PADDAS, PRCA.

Abstract

The RNA-binding protein Pumilio1 (PUM1) is associated with distinct diseases: a mild, late-onset ataxia and a severe, wide-ranging neurodevelopmental syndrome. The ataxia patients retain 75% of normal PUM1 levels, the syndromic patients ~50%, but why this should cause such different phenotypes was unclear. Target dysregulation did not explain the difference, so we developed a PUM1 interactome for the mouse brain. This revealed RNA-binding proteins involved in aspects of RNA metabolism not previously associated with PUM1 (e.g., alternative splicing), as well as proteins in unexpected pathways (e.g., cyclosome). We focused on a subset of RNA-binding proteins and found that the effects of PUM1 loss on these proteins and their targets varied with brain region and sex. In patient cells, mice, and *in vitro*, mild PUM1 loss affected only PUM1-specific targets, whereas PUM1 haploinsufficiency destabilized these native complexes and altered expression of shared targets. We propose that dosage sensitivity can involve distinct mechanisms, and that there may be more intimate coordination among RNA-binding proteins than is readily evinced by more traditional *in vitro* approaches.

Impact statement

Most studies of RNA-binding proteins focus on identifying their targets, but identifying their protein

partners *in vivo* provides important insights into their functions and loss of function.

Introduction

To respond with agility to a specific perturbation, cells must modify their protein repertoire, much of which is controlled at the post-transcriptional level by RNA-binding proteins (RBPs). RBPs regulate RNA localization, transport, translation, splicing, and decay, and they orchestrate hundreds of pathways that are responsible for proper biological functions (Hentze *et al*, 2018; Keene, 2007b). RBPs can coordinate or compete with each other or exert mutual influence (Dassi, 2017), and they also interact with microRNAs (miRNAs), which are small non-coding RNAs that suppress the expression of their target genes by binding to a short complementary seed region in the 3' UTRs of mRNAs. The RBP and microRNA machinery are particularly important in neurons, whose plasticity demands a rapid local (axonal) response to stimuli despite distance from the nucleus (Mauger *et al*, 2016). Disruptions in RBP function underlie several complex neurological disorders: for example, large CAG expansions in FMRP cause Fragile X syndrome, but milder "premutations" in FMRP cause adult-onset Fragile X-associated tremor and ataxia syndrome (FXTAS) (Lukong *et al*, 2008). The RBPs TDP43 and FUS are both involved in amyotrophic lateral sclerosis, with TDP43 mutations also linked to frontotemporal dementia (Humphrey *et al*, 2020; Ravanidis *et al*, 2018). Despite recent interest in these and other RBPs implicated in neuronal function, we still know relatively little about RBP interactions and regulation (Darnell & Richter, 2012; Khalil *et al*, 2018; Ravanidis *et al.*, 2018).

We recently discovered that the RBP Pumilio1 (PUM1) is involved in two distinct human diseases (Gennarino *et al*, 2018; Gennarino *et al*, 2015). PUM1-associated developmental delay and seizures (PADDAS) is a wide-ranging neurodevelopmental disorder, while PUM1-related cerebellar ataxia (PRCA) is a slowly progressive, pure ataxia with onset in mid-life. Although the severity of the PRCA and PADDAS phenotypes tracks with the levels of functional PUM1 (75% of wild-type levels in PRCA, 40-60% in PADDAS), precisely what is happening at the molecular level was unclear. PUM1 comprises a highly conserved RNA-binding domain composed of eight tandem repeats known as Puf homology domains (HDs), and the mutation that produces mild disease (PRCA), T1035S, lies within this domain and impairs RNA binding—but the most severe PADDAS mutation (R1147W) is outside this domain and does not seem to impair RNA binding (Gennarino *et al.*, 2018; Gennarino *et al.*, 2015). Moreover, the PADDAS phenotype is wide-ranging and variable. The most severe mutation, R1147W, causes small stature, physical dysmorphologies, cognitive and language delays, motor impairments, and seizures starting in infancy. The enormous difference in phenotypic outcomes between mutations in the RNA-binding domain and outside of it, plus the fact that the six then-known PUM1 targets were

67 upregulated to similar extents in the PRCA and PADDAS patient cell lines (Gennarino *et al.*, 2018), led
68 us to hypothesize that PRCA is caused by deregulation of PUM1 targets, but that PADDAS results from
69 disruption of PUM1's interactions with its protein partners along with de-repression of the targets of these
70 complexes.

71 To test this hypothesis would require identifying PUM1 interactors in the mouse brain. Although a
72 great deal is known about the PUMILIO/FBF (PUF) family of RBPs, of which PUM1 and its homolog
73 PUM2 are members, surprisingly little is known about PUM1 function in the postnatal mammalian brain.
74 PUM1 was initially discovered in *Drosophila* for its contributions to embryonic patterning (Lin &
75 Spradling, 1997) and stem cell maintenance (Leeb *et al*, 2014). Studies in fly, worm, and germ cells show
76 that Pumilio proteins regulate mRNA targets through at least three distinct mechanisms: they can
77 collaborate with the miRNA machinery to repress targets (Friend *et al*, 2012; Kedde *et al*, 2010; Miles *et*
78 *al*, 2012); they can recruit the CCR4-NOT deadenylase complex to shorten poly(A) tails and promote
79 mRNA degradation (Temme *et al*, 2014; Van Etten *et al*, 2012; Weidmann *et al*, 2014); and they can
80 antagonize poly(A)-binding proteins to repress translation (Goldstrohm *et al*, 2018). PUM1/2 can also
81 activate certain mRNAs (Bohn *et al*, 2018; Uyhazi *et al*, 2020).

82 Protein interactions in general, and those of PUF family members specifically, can be organism-,
83 transcript-, and even condition-specific (Miller & Olivas, 2011). We therefore took an unbiased approach
84 by using *in vivo* proteomics to identify PUM1's native partners. Because *Drosophila* studies show that
85 Pumilio can change its protein partners in different neuronal types (Muraro *et al*, 2008), we first examined
86 the brain as a whole and then repeated our analyses in three brain regions that most highly express PUM1.
87 We then determined the effect of PUM1 loss on a focused subset of RBP interactors that were the most
88 highly connected within the interactome, using *PUM1* heterozygous and knockout mice and patient-
89 derived cell lines. We also identified targets shared among these interactors and examined their responses
90 to PUM1 insufficiency in mice and cell lines from patients bearing the T1035S and R1147W mutations.
91 Our results support our hypothesis and underscore the need to examine all the interactions an RBP
92 engages in, not just its targets. (Note that, because we deal with both mouse and human proteins in this
93 paper, we will refer to the mouse proteins with lower case (e.g., Pum1) and the human proteins in all caps
94 (PUM1).)
95

96 **Results**

97 **Establishing the Pumilio1 interactome across the adult mouse brain**

98 To identify Pum1 protein partners, we performed co-immunoprecipitation (IP) for Pum1 on whole
99 brains from 10-week-old wild-type mice, followed by liquid chromatography with tandem mass

100 spectrometry (LC-MS/MS, or simply mass spec); we used IP against IgG (IP-IgG) as a negative control
101 (see Materials and Methods). Because of the intrinsic variability of the mass spec technique, we combined
102 and homogenized whole brains from two 10-week-old wild-type mice per sample (1 female and 1 male),
103 aliquoting half of each sample for IP against either Pum1 or IgG, then performed six biological replicates
104 (six samples, 12 mice total) for each mass spec experiment against IP-Pum1 and IP-IgG. Post-IP western
105 blot detected no residual Pum1 from brain tissue, confirming that our protocol recovers virtually all of
106 Pum1 (**Figure 1–figure supplement 1A**).
107 Principal component analysis (PCA) readily separated the IP-Pum1 interactors from the control IP-
108 IgG (**Figure 1–figure supplement 1B**). To increase the likelihood that our candidates would prove to be
109 genuine interactors, the proteins had to have at least two unique peptides present in at least five out of six
110 IP-Pum1 samples and also show at least an average >1.5-fold difference between IP-Pum1 and IP-IgG in
111 label-free quantification intensity (LFQ-intensity, see Materials and Methods). Our analysis yielded 412
112 putative Pum1 interactors (**Figure 1A** and **Supplementary Table 1**). We incorporated mammalian
113 protein-protein interaction data from CORUM and the Human Protein Atlas by using g:GOSt (g:Profiler;
114 see Materials and Methods) (Raudvere *et al*, 2019) to reveal 22 clusters of functionally related proteins
115 (**Figure 1A**). Among the putative interactors were those that have been previously identified, supporting
116 the validity of our approach. For example, our mass spec identified Nanos1, the mammalian homologue
117 of *Drosophila* Nanos, which was one of the first proteins found to interact with Pumilio during fly
118 development (Wang *et al*, 2001); it also identified Pum2 and Fmrp, which associate with Pum1 in neural
119 progenitor cells (Zhang *et al*, 2017). Some of the identified proteins belong to families previously found
120 to interact with PUM1 *in vitro*, such as Cnot1, which is the central scaffold of the CCR4-NOT complex
121 (Enwerem *et al*, 2021; Van Etten *et al.*, 2012). Translation initiation factors (cluster 3) have been found to
122 cooperate with Puf proteins in other species (Blewett & Goldstrohm, 2012), and human PUM2-mediated
123 repression was found to require PABPC1, while our mass spec yielded Pabpc4 (Weidmann *et al.*, 2014).
124 Nanos1 and Pabpc4 have numerous connections among the clusters. Cluster 8, which includes proteins
125 that have been associated with RNA fate regulation, was the most strongly interconnected with other
126 clusters.
127 Most of the proteins, of course, have never been associated with PUM1. Among the candidate
128 interactors with the greatest fold-change were many members of the anaphase-promoting complex
129 (cluster 21). This E3 ubiquitin ligase complex targets substrates for degradation and is essential for
130 neuronal survival (Almeida *et al*, 2005; Gieffers *et al*, 1999; Sivakumar & Gorbsky, 2015). We performed
131 preliminary validation by reciprocal co-IP between Pum1 and Anapc1, which scaffolds the APC/C
132 complex, and between Pum1 and Fzr1, which forms its catalytic pocket (Sivakumar & Gorbsky, 2015)

133 (**Figure 1–figure supplement 1C, D**). Cluster 11 was also unexpected, as it contains members of both
134 mTORC1 (Rptor, Cad, Tsc1, Tsc2) and mTORC2 (Rictor) pathways, which are involved in a variety of
135 cellular functions from promoting cell growth to autophagy (Liu & Sabatini, 2020). Reciprocal co-IP with
136 Rptor and Cad confirmed interactions with Pum1 (**Figure 1–figure supplement 1C, D**).
137 Given the plethora of putative interactors to investigate, we repeated the mass spec experiments on
138 the cerebellum, hippocampus, and cortex, where Pum1 is most highly expressed (Gennarino *et al.*, 2015),
139 to see which pathways emerged as predominant. Because our mass spec protocol requires at least 5 mg of
140 protein, we combined cerebellar tissue from eight 10-week-old wild-type mice (4 female and 4 male),
141 performing the experiment in triplicate (for a total of 24 mice); we did the same for cortical tissue. For the
142 hippocampus, we combined tissues from ten wild-type mice (5 of each sex) for three experiments (30
143 mice; see Materials and Methods). As before, we selected proteins with at least two unique peptides and
144 an average of >1.5 fold-change between IP-Pum1 and the IP-IgG. PCA again showed a clear separation
145 of Pum1 samples from the IgG and indicated that the Pum1 hippocampal and cortical interactomes are
146 more similar to each other than to that of the cerebellum (**Figure 1–figure supplement 2A**). We
147 identified 854 putative Pum1 interactors in the cerebellum, 423 in the hippocampus, and 598 in the cortex
148 (**Supplementary Table 1**). 467 were unique to the cerebellum, 140 to the hippocampus, 229 to the
149 cortex, and 154 unique to the rest of the brain (i.e., excluding these three regions). Only 88 candidates
150 were shared among these three brain regions and the whole brain (**Figure 1–figure supplement 2B**,
151 yellow dots; **Figure 1–figure supplement 2C**). To our surprise, the only brain region to show interaction
152 between Pum1 and Pum2 was the cortex (**Figure 1–figure supplement 2C**).
153 The region-specific proteins expanded the list of Pum1 interactors in the pathways described initially
154 (**Figure 1–figure supplement 2D-F**). For example, Cnot1 and Cnot2 turned up in all three brain regions,
155 but Cnot10 appears to be cortex-specific (**Figure 1–figure supplement 2F**). There were many proteins
156 involved in translation initiation, with Eif3b being specific to the hippocampus (**Figure 1–figure**
157 **supplement 2B**). Rbfox1 was specific to the cortex, and Rbfox2 to the cerebellum (**Figure 1–figure**
158 **supplement 2B**), consistent with previous work showing that Rbfox1 mediates cell-type-specific splicing
159 in cortical interneurons (Wamsley *et al*, 2018) and that Rbfox2 is needed for cerebellar development
160 (Gehman *et al*, 2012). The brain-region-specific analysis did not yield many additional interactors in the
161 APC/C (**Figure 1–figure supplement 2D**) or mTOR pathways (**Figure 1–figure supplement 2E**). It did,
162 however, reveal many pathways that have never been associated with Pum1 (**Supplementary Table 1**).
163 Taken as a whole, these data suggest that the RNA-silencing, CCR4-NOT, translational initiation, polyA
164 regulation, and splicing machineries are fine-tuned according to brain region or neuronal cell types,
165 whereas the APC/C and mTOR machineries remain fairly consistent, at least across these three brain

166 regions.

167 This is not to say that certain interactions are necessarily limited to these brain regions. They may
168 occur in regions not tested; they may occur across the whole brain, but at levels that did not reach the
169 threshold we set. It could also be that some interactors are expressed more highly in specific brain
170 regions, though this is not the determining factor for the interaction with Pum2, which is expressed to an
171 equivalent degree in all three brain regions (**Figure 1–figure supplement 2G**).

172 We then performed DAVID Gene Ontology analysis for the hits from both the whole brain and each
173 brain region (**Figure 1B** and **Supplementary Tables 2**). The dominant categories were ubiquitin ligases
174 (anaphase-promoting complex [APC/C], E2/E3 and Kll-linked ubiquitin) and RBPs involved in various
175 aspects of RNA metabolism (RNA silencing, 3'UTR binding, mRNA stability, transport, and splicing).
176 We decided to prioritize the RBPs in cluster 8 (**Figure 1A**)—Fmrp and Ago2 (involved in RNA
177 silencing), Pum2, Cnot1, and Rbfox3 (an alternative splicing factor)—for three reasons. First, this cluster
178 was the most highly interconnected with other clusters; second, RNA-related categories were prominent
179 in the gene ontology analyses for both whole brain and all three brain regions; and third, these RBPs have
180 been well studied and would allow us to more readily test the consequences of PUM1 loss.

181

182 **Pum1 associates with Pum2, Fmrp, Ago2, and Cnot1 in the absence of mRNA**

183 We first performed co-IP followed by western blot to confirm Pum1 association with Pum2, Fmrp,
184 Ago2, Rbfox3 and Cnot1 (**Figure 2A**, *left panel*). Because Fmrp and Ago2 both bind Mov10 *in vitro*
185 (Kenny *et al*, 2020; Kenny *et al*, 2014), we also blotted for murine Mov10, even though it did not appear
186 among our mass spec results. Mov10 was pulled down with Pum1, likely in concert with Fmrp (**Figure**
187 **2A**). Reciprocal co-IP using antibodies against Pum2, Ago2, Fmrp, Rbfox3, Cnot1, and Mov10 followed
188 by western blot confirmed these associations (**Figure 2B**). To verify the specificity of the antibodies, we
189 co-IPed Pum1 and blotted for all six RBPs in *Pum1*$^{-/-}$ mouse brain and detected none of them (**Figure 2–**
190 **figure supplement 1A**). As negative controls, we tested other proteins associated with the RISC complex
191 (Ago1 and Ago3) that did not appear in our mass spec data, and our co-IP experiments found no
192 interactions (data not shown).

193 To exclude the possibility that the co-IPs simply recovered other proteins that are co-bound to target
194 RNAs but are not part of the same complex as the protein of interest, we treated the mouse brain samples
195 with RNase and verified that no detectable RNA remained (see Materials and Methods). Pum1 still
196 associated with Pum2, Fmrp, Ago2, and Cnot1 in the absence of mRNA, but not Rbfox3 or Mov10
197 (**Figure 2A**, *right panel*). Interestingly, a previous *in vitro* study observed PUM1 interaction with AGO2
198 only in the presence of RNA in T-REx 293 cells (Sternburg et al., 2018). We repeated the RNase

199 experiments in HEK293T cells, which confirmed our results (except for RBFOX3, which was not
200 detectable in these cells) (**Figure 2C**).
201
202 **Some interactions among these RBPs require PUM1**
203 We next performed reciprocal co-IP in wild-type and *Pum1*$^{-/-}$ 10-week-old mouse brains for Pum2,
204 Ago2, Fmrp, Cnot1, Rbfox3, and Mov10. Pum2 interacted with Cnot1 only in the presence of Pum1
205 (**Figure 3A**). Unexpectedly, Fmrp associated with Mov10 and Rbfox3 only in the presence of Pum1
206 (**Figure 3B-D**). Fmrp and Cnot1 did not associate in the wild-type brain (**Figure 3B**, *left*) but they did so
207 in the absence of Pum1 (**Figure 3B**, *right*). Ago2 associated with Pum1, Fmrp, Cnot1 and Mov10 in wild-
208 type brain, but in the absence of Pum1 it no longer interacted with Fmrp or Mov10 (**Figure 3E**). Mov10
209 associated with Fmrp but not with Ago2 (**Figure 3D** and **E**). Rbfox3 associated with Cnot1 (**Figure 3C**)
210 but not *vice versa* (**Figure 3F**). IPs against Pum2, Ago2, Fmrp, Cnot1, Rbfox3, and Mov10 with and
211 without RNase treatment in wild-type and *Pum1*$^{-/-}$ mouse brains (**Figure 3–figure supplement 1A-F**)
212 confirmed that, in the absence of Pum1, these interactions require RNA.
213 These results underscore the importance of examining RBP interactions *in vivo*, in specific contexts,
214 with and without RNase treatment. For example, previous work showed that AGO2, PABPC1, GW182
215 and CNOT1 interact with nuclear EGFR to regulate VEGF signaling in tumor cell lines (Dittmann *et al*,
216 2017), but neither GW182 nor EGFR turned up in either our whole-brain or regional interactomes. In fact,
217 none of GW182's three mammalian paralogues (Tnrc6A, Tnrc6B, or Tnrc6C), which interact with all
218 four human AGO proteins, was pulled down in our mass spec against Pum1 (**Supplementary Table 1**).
219 In murine neurons, therefore, Pum1 associates with Pum2, Fmrp, Ago2, and Cnot1, with or without
220 RNA (**Figure 3A-F** and **Figure 3–figure supplement 1A-F**). Pum1 seems to be required for association
221 between Fmrp, Mov10 and Rbfox3, and between Ago2 and Fmrp, Mov10, and Cnot1. In the absence of
222 Pum1, the associations between Pum2, Fmrp, Ago2 and Cnot1 require RNA (**Figure 3–figure**
223 **supplement 1A-F**).
224
225 **Pum1 loss alters RBP levels by brain region and sex**
226 If these are *bona fide* interactors of Pum1, then we would expect loss of Pum1 to alter their
227 abundance. *Pum1* heterozygous and knockout mice showed changes in the quantities of Pum2, Ago2, and
228 Mov10 proteins across the brain (**Figure 4–figure supplement 1A**), but only *Pum2* showed changes in
229 mRNA levels (**Figure 4–figure supplement 1B**). Interestingly, Ago2 and Mov10 levels fell only in male
230 mice (**Figure 4–figure supplement 1A**), so we decided to pursue this sex difference by brain region. We
231 quantified Pum2, Fmrp, Ago2, Rbfox3, Cnot1 and Mov10 in the cerebellum, cortex, and hippocampus.

232 We first measured Pum1 mRNA and protein levels to confirm the reduction of Pum1 in our *Pum1*$^{+/-}$ or
233 *Pum1*$^{-/-}$ mice in each brain region (**Figure 4A-C,** and **Figure 4–figure supplement 2A**). Pum2 protein
234 levels rose in all three brain regions, as did its mRNA (**Figure 4A-C,** and **Figure 4–figure supplement**
235 **2A**).
236 Fmrp protein expression was upregulated in all three brain regions in male KO mice, but in female
237 KO cerebella Fmrp was reduced by almost 70% (**Figure 4A**). (We should note that sex differences in
238 Fmrp expression have been previously reported (Singh *et al*, 2007; Singh & Prasad, 2008).) Three other
239 proteins also showed divergent responses to Pum1 loss according to sex and brain region: Ago2 (up in
240 female but down in male cerebella, with the opposite pattern in hippocampus and cortex), Rbfox3 (in the
241 hippocampus), and Cnot1 (in the cerebellum) (**Figure 4A-C**). None of them showed any changes in
242 mRNA levels (**Figure 4–figure supplement 2A**), despite the fact that *Fmr1* and *Cnot1*, like *Pum2*, have a
243 Pumilio Response Element (PRE) (Zamore *et al*, 1997)—sometimes known as a Pumilio Recognition
244 Element (PRE) or Pumilio Binding Element (PBE)—in their 3'UTR. It may be that the loss of Pum1
245 causes sex- and region-specific reorganization of these complexes, or that there are additional sex-specific
246 Pum1 interactors.
247
248 **Pum1 loss dysregulates Ago2 and the microRNA machinery in mouse cerebella by sex**
249 Since loss of Pum1 function has deleterious effects on the cerebellum in both mice (Gennarino *et al.*,
250 2015) and humans (Gennarino *et al.*, 2018), we were curious to know whether the divergence of Ago2
251 protein levels in males and females extended to cerebellar miRNAs. We performed miRNAseq.
252 Hierarchical heatmap clustering of miRNA expression in *Pum1*$^{-/-}$ and WT male and female cerebella at 10
253 weeks of age revealed that the expression of 166 miRNAs (**Supplementary Table 3**) diverged between
254 the two sexes in parallel with Ago2 expression (**Figure 4D**).
255 To examine the functional consequences of this Ago2/miRNA dysregulation, we looked at the
256 expression of downstream targets that are co-bound by those miRNAs in 10-week-old wild-type and
257 *Pum1*$^{-/-}$ male and female cerebella. We first selected all the miRNAs with at least a 25% change in
258 expression in either direction, for a total of 19 miRNAs. Using TargetScan and CoMeTa (Agarwal *et al*,
259 2015; Gennarino *et al*, 2012) we identified 6832 putative targets that are co-bound by at least 2 out of 19
260 possible miRNAs. To reduce this list to a more manageable size for testing expression changes by qPCR,
261 we prioritized targets that are co-bound by at least 8 miRNAs, for a total of 49 putative targets. *Pum1*$^{-/-}$
262 male and female cerebella showed gene expression changes for 44 out of these 49 targets, which
263 correlated with the sex-dependent differences in Ago2 levels (**Figure 4E**, **Figure 4–figure supplement**
264 **2B** and **Supplementary Table 4**).

265

266 **The top targets of Pum1, Pum2, Fmrp, Ago2, and Rbfox3 are shared**

267 So far our *in vivo* proteomics results seem to be borne out by changes in the levels of protein
268 interactors upon loss of Pum1. Ideally, we would purify recombinant proteins to perform gel filtration
269 assays to get a better handle on the nature of the interactions, but Pum1 is difficult to purify because it is
270 prone to aggregation (Miller & Olivas, 2011). If the complexes Pum1 forms with these RBPs are
271 physiologically relevant, however, then they should co-regulate at least some of the same mRNA targets.
272 Indeed, one corollary of the "regulon theory," which posits that mRNA targets in the same pathway are
273 co-regulated (Blackinton & Keene, 2014; Keene, 2007a, b; Keene & Lager, 2005), is that there should be
274 a discernible set of RBPs that do the co-regulating.

275 To test this hypothesis, we downloaded and reanalyzed all the high-throughput sequencing UV-
276 crosslinking and immunoprecipitation (HITS-CLIP) data that is available from the murine brain.
277 Fortunately, this data exist for Fmrp (Maurin *et al*, 2018), Ago2 (Chi *et al*, 2009), Rbfox3 (Weyn-
278 Vanhentenryck *et al*, 2014), Pum1, and Pum2 (Zhang *et al.*, 2017). Then, to determine whether and how
279 much the targets overlap, we performed gene set enrichment analysis (GSEA) (Subramanian *et al*, 2005).
280 GSEA is a method for determining whether members of a particular class of genes from set *S,* such as the
281 targets of a particular RBP like Pum1, are randomly distributed throughout another gene set list *L*, which
282 is ranked (in this case) according to reads per kilobase of transcript, per million mapped reads (RPKM).
283 Genes from *S* that are enriched (over-represented) at the top of *L* are expressed more than would be
284 expected; the converse is true for genes over-represented at the bottom of *L*. Here, we performed pairwise
285 GSEA analysis using Fmrp as the basis for comparison (because it has the largest dataset) and Pum1,
286 Pum2, Ago2 and Rbfox3. As negative controls, we used HITS-CLIP data from mouse brain for four
287 RBPs that did not show up as Pum1 interactors in our mass spec: Mbnl2 (Charizanis *et al*, 2012), Nova
288 (Zhang *et al*, 2010), Apc (Preitner *et al*, 2014), and Ptpb2 (Licatalosi *et al*, 2012).

289 Strikingly, Pum1 HITS-CLIP targets were preferentially distributed in the top 5th percentile of all
290 Fmrp targets, with an enrichment score (ES) of 0.93 (the maximum is 1) and a FDR of 0 (**Figure 5A,** *blue*
291 *line represents ES*). Pum2, Ago2, and Rbfox3 showed nearly identical patterns (**Figure 5A**). There was
292 no significant overlap between the targets of Fmrp and those of any negative control (Nova had the
293 highest ES, but this was only 0.36 with a rank max of 45th percentile and FDR=1; **Figure 5B**).

294 To ascertain whether the highest-ranking Fmrp targets correspond to the genes with the highest
295 probability of being Pum1 targets, we performed a more detailed GSEA. We first divided the Fmrp
296 ranked target list into 10 equal bins according to percentile. We then repeated GSEA of Pum1 HITS-CLIP
297 data for each bin and found that 648 of the 1194 identified Pum1 targets (54%) are in the top 10th

298 percentile of Fmrp targets, with an ES of 0.8; moreover, this was the only statistically significant bin
299 (**Figure 5C**). This was also true for Pum2, Ago2, and Rbfox3 (**Figure 5C**). Neither Pum1, Pum2, Rbfox3,
300 Fmrp, nor Ago2 targets were enriched among any of the target lists of the negative controls ranked by
301 RPKM (**Figure 5–figure supplement 1A,** and data not shown).
302 We then performed the corresponding analysis using the Pum1 target list as the basis for comparison
303 instead of the Fmrp list. We ran GSEA on each of the four Pum1 partners against the list of Pum1 target
304 genes (again ranked by RPKM), and each partner's targets are within the top 20% of the Pum1 list
305 (**Figure 5D**). Specifically, Fmrp's targets reside in the top 10th percentile (with an ES of 0.81), Pum2's
306 targets within the 16th percentile (ES=0.9), Ago2's targets within the 18th percentile (ES=0.76), and
307 Rbofx3's targets within the 19th percentile (ES=0.67). The four RBPs used here as negative controls have
308 a minimum rank at the 37th percentile, and the best ES was 0.26 for Apc; none of the five reached
309 statistical significance (**Figure 5D**). These analyses demonstrate that there is substantial overlap among
310 the highest-ranked targets of Pum1, Pum2, Fmrp, Ago2, and Rbfox3.
311 We then decided to look at the targets shared by Pum1, Pum2, Ago2, and Rbfox3 and see how they
312 distribute within Fmrp. The result was striking, with an ES of 0.93 falling within the top 5th percentile
313 (**Figure 5E**); 141 out of 175 common targets were within the top 10th percentile (bin 1) of Fmrp targets,
314 with 99 within the top 5th (**Figure 5F** and **Supplementary Table 5**). This contrasts with the negative
315 controls, for which the best ES was 0.41 within the top 40th-60th percentile (**Figure 5G**). DAVID gene
316 ontology analysis of those 175 common targets between Ago2, Pum1, Pum2, Fmrp, and Rbfox3 revealed
317 pathways enriched in neurons and axonal projections (**Figure 5–figure supplement 1B** and **C**). Previous
318 studies have shown that Pum1 and Pum2 cooperate with the microRNA machinery to suppress certain
319 targets (Gennarino *et al.*, 2015; Kedde *et al.*, 2010). Among Fmrp HITS-CLIP targets, there were almost
320 300 microRNAs. Pum1 HITS-CLIP has 60 miRNAs, only four of which are not shared with Fmrp; Pum2
321 HITS-CLIP has no miRNAs that are not shared with either Pum1 or Fmrp (**Figure 5–figure supplement**
322 **1D** and **Supplementary Table 6**).
323 Because neuronal genes tend to be long (Zylka *et al*, 2015) and RPKM can introduce bias toward
324 longer genes (Mandelboum *et al*, 2019), we wanted to ensure that the targets were actually more highly
325 expressed. Since the published HITS-CLIPs data from other studies were acquired from mice at different
326 ages (but most at 3 weeks of age) and these studies did not typically perform RNAseq in parallel with
327 HITS-CLIP from the same tissue and age, we decided to perform RNAseq from WT mice at 3 weeks of
328 age in triplicate to determine a baseline level of gene expression in mouse brain expressed as DESeq2-
329 normalized counts (Love *et al*, 2014) (see Materials and Methods and **Supplementary Table 7**). We then
330 normalized RPKM values and repeated the GSEA enrichment analysis. The enrichment between the

331 targets of Pum1 and those of Pum2, Ago2, Fmrp, and Rbfox3 was retained even after gene expression
332 normalization (**Figure 5–figure supplement 1E-G**), with a minimum ES of 0.78, while the maximum
333 score of the negative controls was 0.38 (**Figure 5–figure supplement 1E, F**). The shared targets of
334 Pum1, Pum2, Rbfox3, and Ago2 were even more enriched, with an ES of 0.84 (**Figure 5–figure**
335 **supplement 1H**).
336
337 **PUM1 interactors are destabilized in cell lines from PADDAS, but not PRCA, patients**
338 Having identified PUM1 interactors and shared targets, we were now in a position to test our two-
339 pronged hypothesis about how *PUM1* mutations can lead to different diseases. To determine whether
340 either mutation destabilizes PUM1 interactors, we compared their levels in patient-derived cell lines with
341 those in controls. For PADDAS, we compared fibroblasts from one 9-year-old female patient (R1147W;
342 subject 1, or S1) with fibroblasts from three different 9-year-old female healthy controls. For PRCA, we
343 compared lymphoblastoid cells from two female PRCA patients (both with the T1035S mutation; subjects
344 2 and 3, or S2 and S3, 59 and 58 years old, respectively) with lymphoblastoid cells from three different
345 58-year-old female healthy controls (Gennarino *et al.*, 2018). We first measured how much PUM1 we
346 could pull down from the patient-derived cell lines compared to their respective controls. Post-IP did not
347 detect any residual PUM1 from PADDAS or PRCA cell lines, or their controls, confirming that our
348 protocol was able to pull down virtually all of the PUM1 protein from patient-derived cell lines (**Figure**
349 **6–figure supplement 1A, B**). IP against PUM1 followed by western blot showed that PADDAS cells had
350 49%, and PRCA cells 76%, of the amount of PUM1 found in healthy controls (**Figure 6A** and **B**),
351 consistent with our previous report (Gennarino *et al.*, 2018).
352 Co-IP confirmed that PUM1 associates with PUM2, FMRP, AGO2, CNOT1, and MOV10 in patient
353 cell lines (**Figure 6A** and **B**). The mild T1035S variant reduced PUM1 binding to AGO2 by ~21%
354 (**Figure 6B**). The more severe R1147W variant, however, reduced PUM1 association with AGO2,
355 CNOT1, and MOV10 by ~84%, ~59%, and ~90%, respectively (**Figure 6A**). Interaction with FMRP did
356 not appear to be affected. (We could not examine the effect of PUM1 mutations on RBFOX3, which is
357 not expressed in fibroblasts or lymphoblastoid cells.)
358 Western blot analysis revealed that the proteins that lose their association with the R1147W variant
359 undergo reduction in their expression levels (**Figure 6C**). Note that MOV10's association with R1147W
360 was greatly reduced (**Figure 6A**) even though its protein levels were unchanged (**Figure 6C**). AGO2 and
361 CNOT1 levels were unchanged in the PRCA cell line but were ~50% lower in the PADDAS cell line
362 (**Figure 6C**). The mRNA levels of *PUM1*, *AGO2*, *CNOT1*, and *MOV10* did not change (**Figure 6–figure**
363 **supplement 1C**), confirming that the reductions in their respective protein levels were due to the loss of

364 interaction with PUM1-R1147W.

365 One limitation of these studies is that we are implicitly comparing different cell types. Since we
366 haven't been able to procure lymphoblasts from PADDAS patients or fibroblasts from PRCA patients, we
367 sought to confirm our findings *in vitro*. We inserted a GST-tag at the N-terminal of *AGO2*, *CNOT1*, and
368 *FMRP* (see Materials and Methods). (AGO2 and CNOT1 were the only proteins whose levels changed in
369 fibroblasts, so FMRP is used here as a control.) We also cloned a Myc-tag polypeptide at the N-terminal
370 of *PUM1*-WT, *PUM1*-R1147W (PADDAS) and *PUM1*-T1035S (PRCA) (see Materials and Methods).
371 We then co-transfected the same amount of Myc-tagged PUM1 proteins with the GST-tagged interactors,
372 followed by western blot to quantify the amount of GST-tagged protein retrieved relative to the quantity
373 of PUM1 proteins pulled down in the IP. GST-AGO2 associated with Myc-PUM1-R1147W 76% less
374 than it did with Myc-PUM1-WT (**Figure 7A**), in alignment with our observations in the PADDAS cell
375 lines (**Figure 6A, B**). We also found ~35% less interaction with CNOT1 (**Figure 7B**) but no decrease in
376 PUM1 association with FMRP (**Figure 7C**), again in accord with our findings in patient-derived cells
377 (**Figure 6A**, **B**).

378 We also examined the effects of the PUM1 mutant on PABPC1, PABPC4, EIF4A3, and EIF4G3
379 (**Figure 1A**), which various studies have indicated interact with each other (Cheng & Gallie, 2007; Gallie,
380 1998; Le *et al*, 1997) and seems to be important for Pumilio activities but not necessarily as its interactors
381 (Goldstrohm *et al.*, 2018; Menon *et al*, 2004). We cloned a GST-tag at the respective N-terminals and
382 performed the experiment as described above. While the R1147W mutation reduced interaction with
383 PABPC1 by roughly 40%, it actually increased interaction with PABPC4 by 350% (**Figure 7–figure**
384 **supplement 1A** and **B**). Strikingly, PUM1-R1147W increased interaction with EIF4A3 and EIF4G3 by
385 1600% to 2760% (**Figure 7–figure supplement 1C** and **D**).

386 These data suggest that the effects of the R1147W mutation, which does not impair PUM1 binding to
387 mRNA (Gennarino *et al.*, 2018), are due to the loss of interactions with RBPs that repress mRNA with a
388 concomitant gain of function with translational initiation proteins.

389

390 **R1147W mutation dramatically destabilizes PUM1**

391 We next tested the PUM1 variants in a protein stability assay. We measured the half-life of the three
392 Myc-tagged PUM1 proteins by separately transfecting 125ng of each. After cycloheximide treatment (T0)
393 to block translation, we quantified the amount of protein at different time points: 30min, 1h, 2h, 4h, and
394 5h, compared to T0 (**Figure 7–figure supplement 1E**). The half-life of PUM1-WT was roughly 5.5
395 hours, the half-life of
396 PUM1-T1035S was ~2 hours, and that of PUM1-R1147W slightly less than 1 hour (**Figure 7–figure**

397 **supplement 1E**).

398 We also wondered whether the R1147W mutation might be impaired in binding with WT PUM1. It
399 has been thought that Puf proteins do not dimerize (Edwards *et al*, 2001; Zamore *et al*, 1999), but recent
400 work supports this possibility (Qiu *et al*, 2019). We therefore co-transfected each of the Myc-tagged
401 PUM1 variants with the same amount of GST-tagged *PUM1*-WT and used an empty vector as a negative
402 control. First, we confirmed that IP against Myc-PUM1-WT pulled down GST-PUM1-WT. IP against
403 Myc-PUM1-R1147W pulled down 51% of the total GST-PUM1-WT, while the interaction between Myc-
404 PUM1-T1035S and GST-PUM1-WT remained unchanged (**Figure 7D**). The same interaction was
405 observed after RNase treatment, suggesting that mammalian PUM1 dimerizes without RNA (**Figure 7–**
406 **figure supplement 1F**). These data suggest that the R1147W mutation might exert a dominant-negative
407 effect on wild-type PUM1.

408 The combination of lower protein levels and marked protein instability helps explain why the
409 R1147W phenotype is better represented by the *Pum1* null mice than by the heterozygotes (Gennarino *et*
410 *al.*, 2018).

411

412 **Shared targets are upregulated in PADDAS but not PRCA**

413 We had hypothesized that PRCA would involve dysregulation of PUM1 targets, whereas PADDAS
414 would involve both destabilization of PUM1 interactors and dysregulation of downstream targets of those
415 interactors. We therefore tested the effects of the T1035S and R1147W mutations on validated PUM1-
416 specific targets (Chen *et al*, 2012; Gennarino *et al.*, 2015; Zhang *et al.*, 2017) that are not in the HITS-
417 CLIP data for the other RBPs but are expressed in both fibroblasts and lymphoblasts. PUM1-specific
418 mRNA were dysregulated to very similar extents in PRCA and PADDAS patient cells, with only a few
419 targets being up to 20% more upregulated in PADDAS (**Figure 7E**).

420 We then examined the mRNA levels of all 175 targets shared between PUM1, PUM2, AGO2, FMRP,
421 and RBFOX3 (**Figure 5E** and **Supplementary Table 5**) in the same PRCA and PADDAS patient cell
422 lines. Of these shared targets, 55 were expressed in both PADDAS fibroblasts and PRCA lymphoblastoid
423 cells. Of these 55, 52 shared targets were upregulated in PADDAS but not in PRCA (**Figure 7F**), by an
424 average of two-fold (ranging from a low of 121% for IDS to 347% for TLK1). There was little or no
425 change in most of these targets in PRCA cells, though levels of CALM1, ATP2A2, CREB1, and GNAQ
426 fell by ~40%, and CALM2, TAOK1, and UBE2A by ~20% (**Figure 7F**).

427 These results support our hypothesis that the symptoms observed in PRCA are attributable to the
428 dysregulation of PUM1-specific target genes, while PADDAS involves both protein partner
429 destabilization and dysregulation of the partner proteins' targets.

430

431 **Discussion**

432 Since our initial study describing PUM1-related diseases (Gennarino *et al.*, 2018), we and others have
433 identified additional PADDAS and PRCA patients (Bonnemason-Carrere *et al*, 2019; Gennarino *et al.*,
434 2018; Imaizumi *et al*, 2019; Lai *et al*, 2019). In our sample, R1147W accounts for the majority of
435 PADDAS patients, and T1035S for the majority of PRCA, which supports the value of studying these
436 particular two mutations as causing the most severe and the most mild forms of PUM1-related disease.
437 The question that drove the present study is: why should the 25% drop in PUM1 levels from PRCA to
438 PADDAS produce such different phenotypes, especially when R1147W is not impaired in binding to
439 mRNA? Our data strongly support our hypothesis that the difference is not due to a linear increase in the
440 de-repression of mRNA targets but is rather a function of an additional mechanism coming into play: the
441 destabilization of numerous interactions and the de-repression of their downstream targets. We draw this
442 conclusion from several lines of evidence. First, when Pum1 was reduced by 50% (in heterozygous mice)
443 or 100% (in knockout mice), there were changes in the levels of associated proteins that depended on
444 brain region and sex. Second, we found changes in the levels of these proteins in patient cell lines, despite
445 unchanged mRNA levels. Third, our *in vitro* studies using Myc- and GST-tagged proteins showed that
446 AGO2 and CNOT1 lose their interaction with PUM1-R1147W, which itself binds less to WT PUM1.
447 Fourth, not all interactions were diminished: the responses to R1147W ranged from a loss of 40-70% to a
448 gain of 2760%. Together these data persuade us that a 50% loss of PUM1, whether through
449 heterozygosity or the R1147W mutation, disrupts interactions with native partners and differentiates
450 PADDAS from PRCA.

451

452 *Diseases involving dosage-sensitive proteins*

453 There are other dosage-sensitive proteins that produce different phenotypes depending on their
454 expression level (Tan & Zoghbi, 2019), and our results raise the possibility that interacting complexes
455 may be disrupted once expression falls below a certain threshold. What that threshold might be, exactly,
456 is not clear, but for PUM1 it seems to be somewhere between the 75% of wild-type levels of PUM1 seen
457 in PRCA and the 60% level estimated for the R1139W mutation that produced a milder form of PADDAS
458 (Gennarino et al., 2018). In this context it is worth noting that a recent study found that, below a threshold
459 of ~70% of normal levels of FMRP, there were steep decreases in IQ for each further decrement in FMRP
460 levels, even as small as 5-10% (Kim *et al*, 2019). The amount of loss that can be sustained for a given
461 protein would likely depend on its usual quantities, and it is possible that for some proteins, the difference
462 in phenotype between greater and lesser abundance may indeed reflect a linear progression from mild to

463 severe. For example, a mutation in *MECP2* that reduces the protein levels by only 16% causes a mild
464 form of Rett syndrome: the child developed normally until the age of two years, then regressed, lost
465 acquired language and manual skills, and developed hand stereotypies (Takeguchi *et al*, 2020). She
466 eventually regained the ability to repeat words in an echolalic fashion and never developed seizures, but
467 the phenotype was clearly Rett syndrome. The relationship between protein levels and disease features in
468 MeCP2-related disorders may be more linear because this protein is so extraordinarily abundant
469 (Sandweiss *et al*, 2020). Similarly, in proteopathies such as Alzheimer's or Parkinson's disease, genetic
470 duplications of *APP* or *SNCA* cause earlier onset of what is recognizably the same disease (Chartier-
471 Harlin *et al*, 2004; Rovelet-Lecrux *et al*, 2006).
472 In contrast, there are diseases in which the phenotypes do not simply range from mild to severe
473 versions of the same symptoms, but seem to take on a different character. The polyglutamine diseases,
474 such as Huntington's disease and the spinocerebellar ataxias, come to mind, perhaps because it was
475 through studying spinocerebellar ataxia type 1 (SCA1), that PUM1's role in neurological function was
476 discovered (Gennarino *et al.*, 2015). In the polyglutaminopathies, the disease-causing protein bears an
477 abnormally expanded CAG tract that tends to expand upon intergenerational transmission. Although the
478 range of normal and pathogenic repeat tract lengths differs from one polyglutamine disease to another,
479 larger expansions are more unstable, cause earlier onset, and affect far more tissues than smaller
480 expansions (Orr & Zoghbi, 2007). For example, adult-onset SCA7 presents as ataxia, but infantile SCA7
481 affects the entire nervous system, the heart, and the kidneys, and leads to death by two years of age (Bah
482 *et al*, 2020). Another example is Huntington's disease, where the juvenile form frequently lacks the
483 classic chorea yet produces seizures, which are not a feature of the adult-onset disease; brain
484 morphometry is also quite different in adult- and juvenile-onset cases (Tereshchenko *et al*, 2019). In this
485 family of diseases, therefore, the mechanism is technically the same—repeat expansion—but different
486 tissues have different thresholds for the CAG repeats. In the case of PUM1-related disease, it seems that
487 an additional mechanism comes into play for the more severe phenotypes, beyond upregulation of mRNA
488 targets. Interestingly, FMRP, which harbors a dynamic CGG repeat, is also associated with very different
489 diseases, through two different mechanisms. Very large expansions silence the gene and produce Fragile
490 X syndrome, whereas premutations are thought to cause the adult-onset Fragile-X-associated
491 tremor/ataxia syndrome through RNA toxicity (Salcedo-Arellano *et al*, 2020).
492
493 *Implications of the interactome*
494 It has never been clear how the various modes of action attributed to PUM1 or other RBPs relate to
495 one another, in large part because studies typically focus on one protein or pathway at a time. Our data

496 suggest that the three mechanisms of repression that have been proposed for PUM1 may be coordinated in
497 neurons, insofar as PUM1, PUM2, FMRP, AGO2, MOV10, CNOT1 and RBFOX3 (and related proteins
498 in specific brain regions) either interact or are so close to each other within the ribonucleosome that the
499 loss of Pum1 or RNA can change the composition of the complexes that are identified by co-IP, in ways
500 that are specific to brain region and sex. In this context it is worth noting that a very recent study found
501 alternative splicing is altered in hippocampal slices from Fmrp-deficient mice; this observation was
502 attributed to changes in H3K36me3 levels (Shah *et al*, 2020). Our data suggest that FMRP has an even
503 closer relationship with the RBFOX protein family and alternative splicing machinery than suspected.
504 Indeed, recent work has provided tantalizing glimpses of close interactions among various kinds of RNA
505 metabolism. For example, members of the RBFOX family of proteins may, depending on their interactors
506 (and perhaps cell type, sex, age, and species), be involved in microRNA processing in the nucleus and
507 translation in the cytoplasm (Conboy, 2017). The FMRP/MOV10 complex appears to be involved in
508 regulating translation through miRNA, with evidence that this role may change according to cell type
509 (Kenny *et al.*, 2020). Another study used quantitative mass spec to examine how Fmrp expression levels
510 change with age in the wild-type rat dentate gyrus, and found differences in the levels of myriad proteins;
511 among the 153 proteins with the most significant changes in levels were Pum1, Pum2 and Papbc1
512 (Smidak *et al*, 2017). The region-, sex-, and age-specificity of certain interactions indicates that
513 unraveling RBP interactomes *in vivo* will require considerable finesse.
514 Although we did not pursue the entire interactome here, future studies investigating interactions
515 between PUM1 and members of the mTOR pathway and anaphase-promoting complex should be very
516 fruitful. As we were preparing this work, a new study demonstrated that mTORC1 is involved in
517 postsynaptic responses in hippocampal glutamatergic neurons, whereas mTORC2 modulates presynaptic
518 release (McCabe *et al*, 2020). Given the importance of proteostasis at the synapse—and its failure in
519 many neurological diseases (Zoghbi & Bear, 2012)—the notion that different protein-regulating activities
520 might be coordinated is intuitively appealing.
521 There is still much to be understood about how PUM1 works, and where and how the various
522 RNA metabolic machineries come into contact. The fact that several associations we tested are RNA-
523 independent suggests that certain complexes may form prior to binding mRNA. Could different pools of
524 PUM1 form different complexes that determine whether and where a target is bound? Do the subtle
525 differences between brain regions in the choice of interacting partners from the same pathways influence
526 target choice, activity, or both? Given that mRNA is much larger than proteins, is the quantity of these
527 RBPs so great that they coat the RNA? What other proteins may be involved in 'handing off' an mRNA
528 from one pathway to another? Although we began this study to better understand Pum1 functions in

529 neurons, and thus have been rather Pum1-centric, it is by no means certain that Pum1 is the only protein
530 that links these different molecular machineries. It may be simply the first of several missing links that we
531 didn't realize were missing. Creating RBP interactomes should lead to a more complex yet realistic
532 picture of RBP roles in neuronal function and in neurological disease.
533
534 **Acknowledgments**
535 We thank the patients, their families, and their clinical teams for participating in our study, and the
536 anonymous reviewers for helpful suggestions. We thank Mingyu Cao for help with statistical analyses
537 and U.N. Wasko for starting the cloning procedure with Myc and GST tag sequences *in vitro*. We also
538 thank G. Struhl, V. Ambros, T. Duchaine, G. Karsenty, H. Zoghbi, M. Jovanovic, Y. Giardina, and
539 members of the Gennarino laboratory for helpful discussions and support. This work was supported by
540 the National Institute of Neurological Disorders and Stroke (NINDS; R01NS109858 to V.A.G.); the
541 National Ataxia Foundation/Young Investigator Research Grant (V.A.G.); the Brain & Behavior Research
542 Foundation Young Investigator Award; and the Paul A. Marks Scholar Program, Columbia University
543 Vagelos College of Physicians and Surgeons. This project was also supported by the Genomic and RNA
544 Profiling Core at Baylor College of Medicine and the Bioinformatics Core at the Jan and Dan Duncan
545 Neurological Research Institute. The authors declare no competing interests.
546
547 **Author Contributions**
548 S.B. designed and performed molecular experiments, analyzed and interpreted the data, and drafted the
549 manuscript. N.D.P. performed the qPCR experiments, *in vitro* immunoprecipitation assays, analyzed the
550 data, and edited the manuscript. A.C. performed all the brain region dissections in mice, performed the
551 qPCR experiments and maintained the *Pum1* mutant mouse colony. M.C. performed the cloning
552 experiments. V.L.B. interpreted data and wrote the manuscript. P.P and R.K.S. performed mass
553 spectrometry and helped analyze the data. V.A.G. conceived the study, analyzed and interpreted the data,
554 performed molecular experiments, and wrote the manuscript.
555
556 **Declaration of Interests**
557 The authors declare not competing interests
558
559 **Materials and Methods**
560 **Ethical statement and mouse strains.** All animal procedures were approved by the Institutional Animal
561 Care and Use Committee at Columbia University, New York under the protocol AC-AAAU8490. Mice

562 were maintained on a 12-hr light, 12-hr dark cycle with regular chow and water ad libitum. Pum1 knock-
563 out mice were generated as previously described (Chen *et al.*, 2012). C57BL/6J wild-type mice were
564 purchased from Jackson Laboratory and maintained as described above. For brain dissection, mice were
565 anesthetized with isoflurane, and the brain rapidly removed from the skull and lysed in the appropriate
566 buffer according to the experiment (see Materials and Methods Details).
567
568 **HEK293T cell culture and maintenance.** Human embryonic kidney immortalized 293T (HEK293T)
569 cells were grown in DMEM (GenDepot, #CM002-320) supplemented with 10% of heat-inactivated fetal
570 bovine serum (FBS [GenDepot, #F0901-050) and 1% penicillin/streptomycin (GenDepot, #CA005-010).
571 All cells were incubated at 37 °C in a humidified chamber supplemented with 5% CO_2. HEK293T cells
572 were later processed according to the needs of specific experiments (described below).
573
574 **Patient-derived cell lines: fibroblasts and lymphoblasts.** PADDAS and PRCA patient cell lines are the
575 same as those reported previously (Gennarino *et al.*, 2018). The consent form for each subject specifically
576 allows for sharing of medical information and physical exam findings; the sharing of cell lines from the
577 PADDAS and PRCA subjects and the controls was approved under the Baylor College of Medicine IRB
578 H-34578 and the Columbia University Medical Center IRB-AAAS7401 (Y01M00).
579 Primary fibroblasts from the *PUM1* PADDAS patient and the age- and sex-matched controls were
580 generated as previously described (Gennarino *et al.*, 2018). Briefly, cells were isolated from skin biopsies
581 taken from the patient or age-matched controls using standard methodology (Barch and Association of
582 Cytogenetic Technology, 1991) and placed in a transport medium (Ham's F10, Thermo Scientific,
583 #11550043). The skin specimen was later removed from the transport medium using a sterile technique
584 (in a Class II biohazard cabinet) and transferred to a sterile Petri dish where it was cut into small pieces (<
585 0.5 mm) using sterile scalpel blades. These pieces were transferred to the lower surface of a 25 cm^2
586 culture flask (6-8 pieces per flask) which had been pre-moistened with 1-2 mL of AmnioMAX Complete
587 Medium (Thermo Scientific, #11269016) supplemented with 1% penicillin/streptomycin (GenDepot,
588 #CA005-010). Cell cultures were maintained at 37 °C in a humidified incubator supplemented with 5%
589 CO_2. When cell growth was observed around the edges of the tissue, usually 3 to 5 days later, 2 to 3 mL
590 of AmnioMAX Complete Medium were added. Once growth was established and the tissue was anchored
591 to the flask, another 8 mL of AmnioMAX Complete Medium was added. Thereafter, the medium was
592 renewed every 3 to 4 days until ready for sub-culturing.
593 Lymphoblastoid cells from *PUM1* PRCA patients and the age- and sex-matched controls were
594 generated as previously described (Gennarino *et al.*, 2018). Briefly, lymphoblastoid suspension cell

595 cultures were grown in RPMI 1640 medium (Invitrogen, #11875093) supplemented with 10% heat-
596 inactivated fetal bovine serum (Atlanta Biological, Flowery Branch, #S11195H) and 1%
597 penicillin/streptomycin (GenDepot, #CA005-010). Cell cultures were maintained at 37°C in a humidified
598 incubator supplemented with 5% CO_2. Medium was renewed every 2 to 3 days.
599
600 **Immunoprecipitation experiments using mouse brain tissue.** Mouse brain tissues were gathered from
601 an equal number of 10-week-old male and female mice as follows: whole brains from two mice;
602 hippocampi from ten mice; cerebral cortices from eight mice; and cerebella from eight mice. Each
603 grouping is considered one sample for one experiment. Samples were processed with a dounce
604 homogenizer using a lysis buffer consisting of 200mM $NaCl_2$, 100mM $NaPO_4$, 20mM Hepes pH 7.4, 1%
605 Triton X (which should disrupt all but the strongest protein-protein interactions) and complemented by
606 1X of Xpert Protease and 1X of Phosphatase Inhibitor Cocktail Solutions (GenDepot, #P3100-100,
607 #P3200-020). Following homogenization, the samples were placed on ice for 15 minutes then centrifuged
608 at 14,800 rpm at 4°C for 25 minutes to remove the debris from the supernatant. The supernatant was then
609 moved to 1.5 ml tubes (Beckman microfuge tube #357448) and spun down in a Beckman ultra-centrifuge
610 (Optima Max XP) at 4°C for 25 minutes at 44,000 rpm. 10% of the protein lysate was stored as input and
611 only 1% was loaded for western blot. The protein extract was later divided into two aliquots, one for IP
612 against the protein of interest (antibodies listed below) and the other for IP against IgG, and was then
613 incubated with 30 µL of Dynabeads™ Protein G (Invitrogen, #10004D) and 5 µg of antibody overnight at
614 4°C on a rotisserie tube rotator. The next day, the beads were washed four times with the same lysis
615 buffer used for IP and resuspended in 40µL of elution buffer (consisting of lysis buffer, NuPAGE
616 10X Reducing Agent [Invitrogen, #NP0009], NuPAGE LDS sample buffer at 1X final concentration
617 [Invitrogen, #NP0007]) and boiled at 95°C for 10 minutes before the samples were loaded in the
618 NuPAGE 4%–12% Bis-Tris Gels (Invitrogen, #NP0335BOX & #NP0336BOX) for further resolution and
619 western blot analysis.
620 For the IP with RNase treatment, the beads were resuspended in 400 µL of lysis buffer after the three
621 final washes and divided into two separate 1.5 ml tubes of 200 µL each. To establish the dose required to
622 remove all RNA, we tested different amounts of RNase I (Invitrogen, #EN0602) and found that 4 µL was
623 enough to render RNA undetectable both by denaturing gel and cDNA amplification. The negative
624 control was to go without RNase treatment; both were incubated at 37°C for 15 min on a rotisserie tube
625 rotator. After incubation, all the samples were washed one last time with 500 µL of lysis buffer and then
626 eluted in 20 µL of elution buffer. We used the same protocol for all the IP processed by mass
627 spectrometry.

628 The antibodies used for IP were: goat α-PUM1 (Bethyl Laboratories, #A300-201A), rabbit α-PUM2
629 (Bethyl Laboratories, #A300-202A), rabbit α-FMRP (Abcam Cambridge, #ab17722), rabbit α-AGO2
630 (Abcam Cambridge, #ab32381), rabbit α-NeuN (Thermo Fisher Scientific, #PA5-37407), rabbit α-
631 CNOT1 (Cell Signaling Technology, #44613), rabbit α-MOV10 (Bethyl Laboratories, #A301-571A),
632 rabbit α-RAPTOR (Cell Signaling Technology, #2280), rabbit α-CAD (Bethyl Laboratories, #A301-
633 374A), rabbit α-ANAPC1 (Bethyl Laboratories, #A301-653A), and rabbit α-FZR1 (Thermo Fisher
634 Scientific, #PA5-85303).
635 N.B.: The reason the inputs are separated from the IPs and then collaged is because *in vivo* we load
636 only 1% of the lysate, which we later run off the same blot of the IPs and expose the membrane to see
637 either the input (which usually appears first) or the IPs (which for some of them appear with a longer
638 exposure). This is common practice when working with *in vivo* tissues (De Maio *et al*, 2018) (Lee *et al*,
639 2008) (Rousseaux *et al*, 2018) (Di Grazia *et al*, 2021) (Jin *et al*, 2020) (Lee *et al*, 2020).
640
641 **Immunoprecipitation experiments from HEK293T and patient-derived cell lines.** HEK293T cells
642 and patient-derived fibroblasts or lymphoblastoid cells were lysed by pipetting up and down with a
643 1000µl tip in a lysis buffer consisting of 200mM $NaCl_2$, 100mM $NaPO_4$, 20mM Hepes pH 7.4, 1% Triton
644 X and complemented by 1X of Xpert Protease and 1X of Phosphatase Inhibitor Cocktail (GenDepot,
645 #P3100-100, #P3200-020). The rest of the protocol is the same as described above for mouse brain tissue,
646 except that we used 2.5 µg of primary antibody for IP.
647
648 **Co-Immunoprecipitation in-gel digestion for mass spectrometry.** Immunoprecipitated samples were
649 separated on NuPAGE 4-12% gradient SDS-PAGE (Invitrogen, #NP0335BOX & #NP0336BOX) and
650 stained with SimplyBlue (Invitrogen, #LC6060). Protein gel slices were excised and *in-gel* digestion
651 performed as previously described (Shevchenko *et al*, 2006), with minor modifications. Gel slices were
652 washed with 1:1 Acetonitrile and 100mM ammonium bicarbonate for 30 min then dehydrated with 100%
653 acetonitrile for 10 min until shrunk. The excess acetonitrile was then removed and the slices dried in a
654 speed-vacuum at room temperature for 10 minutes. Gel slices were reduced with 5 mM DTT for 30 min
655 at 56°C in an air thermostat, cooled down to room temperature, and alkylated with 11 mM IAA for 30
656 min with no light. Gel slices were then washed with 100 mM of ammonium bicarbonate and 100%
657 acetonitrile for 10 min each. Excess acetonitrile was removed and dried in a speed-vacuum for 10 min at
658 room temperature and the gel slices were re-hydrated in a solution of 25 ng/µl trypsin in 50 mM
659 ammonium bicarbonate for 30 min on ice and digested overnight at 37 ^{o}C in an air thermostat. Digested
660 peptides were collected and further extracted from gel slices in extraction buffer (1:2 ratio by volume of

661 5% formic acid: acetonitrile) at high speed, shaking in an air thermostat. The supernatants from both
662 extractions were combined and dried in a speed-vacuum. Peptides were dissolved in 3% acetonitrile/0.1%
663 formic acid.
664
665 **Liquid chromatography with tandem mass spectrometry (LC-MS/MS).** The Thermo Scientific
666 Orbitrap Fusion Tribrid mass spectrometer was used for peptide tandem mass spectroscopy (MS/MS).
667 Desalted peptides were injected in an EASY-Spray™ PepMap™ RSLC C18 50cm X 75cm ID column
668 (Thermo Scientific) connected to the Orbitrap Fusion™ Tribrid™. Peptide elution and separation were
669 achieved at a non-linear flow rate of 250 nl/min using a gradient of 5%-30% of buffer B (0.1% (v/v)
670 formic acid, 100% acetonitrile) for 110 minutes, maintaining the temperature of the column at 50 °C
671 during the entire experiment. Survey scans of peptide precursors are performed from 400 to 1500 *m/z* at
672 120K full width at half maximum (FWHM) resolution (at 200 *m/z*) with a 2 x 10^5 ion count target and a
673 maximum injection time of 50 ms. The instrument was set to run in top speed mode with 3-second cycles
674 for the survey and the MS/MS scans. After a survey scan, MS/MS was performed on the most abundant
675 precursors, i.e., those exhibiting a charge state from 2 to 6 of greater than 5 x 10^3 intensity, by isolating
676 them in the quadrupole at 1.6 Th. We used collision-induced dissociation (CID) with 35% collision
677 energy and detected the resulting fragments with the rapid scan rate in the ion trap. The automatic gain
678 control (AGC) target for MS/MS was set to 1 x 10^4 and the maximum injection time was limited to 35ms.
679 The dynamic exclusion was set to 45s with a 10ppm mass tolerance around the precursor and its isotopes.
680 Monoisotopic precursor selection was enabled.
681
682 **LC-MS/MS data analysis.** Raw mass spectrometric data were analyzed using the MaxQuant
683 environment v.1.6.1.0 (Cox & Mann, 2008) and Andromeda for database searches (Cox *et al*, 2011) at
684 default settings with a few modifications. The default was used for first search tolerance and main search
685 tolerance (20 ppm and 6 ppm, respectively). MaxQuant was set up to search with the reference mouse
686 proteome database downloaded from Uniprot (https://www.uniprot.org/proteomes/UP000000589).
687 MaxQuant performed the search for trypsin digestion with up to 2 missed cleavages. Peptide, site and
688 protein false discovery rates (FDR) were all set to 1% with a minimum of 1 peptide needed for
689 identification; label-free quantitation (LFQ) was performed with a minimum ratio count of 1. The
690 following modifications were used for protein quantification: oxidation of methionine (M), acetylation of
691 the protein N-terminus, and deamination for asparagine or glutamine (NQ). Results obtained from
692 MaxQuant were further analyzed using the Perseus statistical package (Tyanova *et al*, 2016) that is part of
693 the MaxQuant distribution. Protein identifications were filtered for common contaminants. Proteins were

694 considered for quantification only if they were found in at least two replicate groups. Significant
695 alterations in protein abundance were determined by ANOVA with a threshold for significance of $P <$
696 0.05 (permutation-based FDR correction). Pum1 protein interactors were later considered if they were
697 found in at least five out of six mass spec experiments for whole brain and in at least two out of three
698 experiments for each respective brain region with a fold-change of >1.5 between LFQ-PUM1-WT and
699 LFQ-IgG-WT (see **Table S1**).
700
701 **Protein-protein interaction map.** The protein-protein interaction map for the whole brain (**Figure 1A)**
702 was generated by Cytoscape (https://cytoscape.org/) (Otasek *et al*, 2019) and the interactions among the
703 Pum1 interactors were inferred from Corum (Giurgiu *et al*, 2019) and the Human Protein Atlas (Thul *et*
704 *al*, 2017) by g:GOSt which is a package of g:Profiler (https://biit.cs.ut.ee/gprofiler/gost) (Raudvere *et al.*,
705 2019). The protein-protein interaction to generate the brain region-specific map (**Figure 1–figure**
706 **supplement 2B**) was generated by Cytoscape.
707
708 **Protein quantification and western blot analysis.** Patient-derived lymphoblastoid, fibroblast cell lines,
709 and control cell lines were collected at 6×10^6 cell confluence and processed for protein extraction. For
710 mouse tissues, we processed either half brain (the other half was processed for RNA extraction, see
711 below) or the entire hippocampus, cortex, or cerebellum for protein extraction. Mouse tissues or cell
712 pellets were subsequently lysed with modified RIPA buffer consisting of 25 mM Tris-HCL, pH 7.6,
713 150 mM NaCl, 1.0% Tween 20, 1.0% sodium deoxycholate, 0.1% SDS, completed with 1X Xpert
714 Protease and 1X Phosphatase Inhibitor Cocktail Solutions (GenDepot, #P3100-100 & #P3200-020). Cells
715 were lysed by pipetting them up and down with a p1000 tip and then placed on ice for 20 min followed by
716 centrifugation at 14,800 rpm at 4°C for 25 minutes. Mouse brain tissues were lysed starting from a 18G 1
717 ½" (Becton Dickson, #305196) and move down to 21G 1 ½" (Becton Dickson, #305167) and finally to
718 26G 1 ½" (Becton Dickson, #305111) syringe needles by pipetting them up and down until the lysate
719 passed through the needle smoothly. Proteins were quantified by Pierce BCA Protein Assay Kit (Thermo
720 Scientific, # PI23225) and the absorbance was measured by NanoDrop OneC (Thermo Scientific).
721 Consequently, proteins were resolved by high resolution NuPAGE 4%–12% Bis-Tris Gel (Invitrogen,
722 #NP0335BOX & #NP0336BOX) according to the manufacturer's instructions. All the blots were
723 acquired on the G:BOX Chemi XX9 machine (Syngene; Frederick, MD) using GeneSys software 1.6.5.0.
724 Gel exposures were determine by the software.
725 Antibodies used for all the western blot experiments were: goat α-PUM1 [1:2500, (Bethyl
726 Laboratories, #A300-201A)], rabbit α-PUM1 [1:2000, (Abcam Cambridge, #ab92545)], rabbit α-PUM2

727 [1:2000, (Bethyl Laboratories, # A300-202A)], rabbit α-FMRP [1:1000, (Abcam Cambridge, #ab17722)],
728 rabbit α-AGO2 [1:1000, (Abcam Cambridge, #ab32381)], rabbit α-NeuN (Rbfox3) [1:1000, (Thermo
729 Scientific, #PA5-37407)], rabbit α-CNOT1 [1:1000, (Cell Signaling Technology, #44613)], rabbit α-
730 MOV10 [1:2000, (Bethyl Laboratories, #A301-571A)], and mouse α-GAPDH [1:10000, (Millipore,
731 #CB1001)].
732
733 **RNA extraction and quantitative real-time PCR (qPCR).** Human fibroblast, lymphoblastoid, and
734 respective control cell lines were harvested at 6 X 10^6 confluence prior to RNA extraction. For mouse
735 tissues, half of the whole brain (the other half was processed for protein extraction, see above) or the
736 entire hippocampus, cortex, or cerebellum were processed for RNA extraction. The RNA was collected
737 for both human cells, mouse brain and brain region tissues using the miRNeasy kit (QIAGEN, # 217004)
738 according to the manufacturer's instructions. RNA was quantified using NanoDrop OneC (Thermo Fisher
739 Scientific). cDNA was synthesized using Quantitect Reverse Transcription kit (QIAGEN, # 205313)
740 starting from 1 µg of RNA. Quantitative RT-polymerase chain reaction (qRT-PCR) experiments were
741 performed using the CFX96 Touch Real-Time PCR Detection System (Bio-Rad Laboratories, Hercules)
742 with PowerUP SYBR Green Master Mix (Applied Biosystems, #A25743). Real-time PCR runs were
743 analyzed using the comparative C_T method normalized against the housekeeping human gene *GAPDH* or
744 mouse *Gapdh*, depending on the experiment (Vandesompele *et al*, 2002).
745
746 **Protein stability assay.** HEK293T cells were seeded in 12-well plates for 24h and then transfected with
747 125 ng of either *PUM1* WT or mutant cDNA and one of the interactors using the jetPRIME Transfection
748 Reagent (Polyplus transfection, #55-132) according to the manufacturer's protocol. After 24 h cells were
749 treated with 0.1 mg/ml of cycloheximide (Fisher Scientific, #AAJ66004XF), which we considered time
750 zero. Cells were later collected after 30min, 1h, 2h, 4h and 5h of treatment and processed for protein
751 extraction and western blot analysis. Antibody: mouse α-Myc antibody [1:2000, (Cell Signaling
752 Technologies, #2276)].
753
754 **MicroRNA library construction and sequencing.** Library preparation and microRNA sequencing was
755 performed by LC Sciences according to the following criteria. Total RNA was extracted from cerebellum
756 of WT and *Pum1*$^{-/-}$ male and female at 10 weeks of age in triplicate, for a total of 12 samples using the
757 miRNeasy kit (QIAGEN, # 217004) according to the manufacturer's instructions. The total RNA quality
758 and quantity were assessed with Bioanalyzer 2100 (Agilent Technologies, Santa Clara) with RIN number
759 > 7.0. Approximately 1 µg of total RNA were used to prepare the small RNA library according to the

760 protocol of TruSeq Small RNA Sample Prep Kits (Illumina, San Diego). Then the single-end sequencing
761 50bp was performed on an Illumina Hiseq 2500 at LC Sciences (Hangzhou, China) following the
762 vendor's recommended protocol.
763
764 **MicroRNA sequencing bioinformatic analysis.** Raw reads were subjected to an in-house program,
765 ACGT101-miR (LC Sciences, Houston) to remove adapter dimers, junk, low complexity, common RNA
766 families (rRNA, tRNA, snRNA, snoRNA) and repeats. Subsequently, unique sequences of 18–26
767 nucleotides in length were mapped to specific species precursors in miRBase 22.0
768 (http://www.mirbase.org/) by BLAST search to identify known miRNAs and novel 3p- and 5p-derived
769 miRNAs. Length variation at both 3' and 5' ends and one mismatch inside of the sequence were allowed
770 in the alignment. The unique sequences mapping to specific species of mature miRNAs in hairpin arms
771 were identified as known miRNAs. The unique sequences mapping to the other arm of known specific
772 species precursor hairpins opposite the annotated mature miRNA-containing arm were considered to be
773 novel 5p- or 3p-derived miRNA candidates. The remaining sequences were mapped to other selected
774 species precursors (with the exclusion of specific species) in miRBase 22.0 by BLAST search, and the
775 mapped pre-miRNAs were further BLASTed against the specific species genomes to determine their
776 genomic locations. The last two were also defined as known miRNAs. The unmapped sequences were
777 BLASTed against the specific genomes, and the hairpin RNA structures containing sequences were
778 predicted from the flank 80 nt sequences using RNAfold software (http://rna.tbi.univie.ac.at/cgi-
779 bin/RNAWebSuite/RNAfold.cgi). The criteria for secondary structure prediction were: (1) number of
780 nucleotides in one bulge in stem (≤12), (2) number of base pairs in the stem region of the predicted
781 hairpin (≥16), (3) cutoff of free energy (kCal/mol ≤-15), (4) length of hairpin (up and down stems +
782 terminal loop ≥50), (5) length of hairpin loop (≤20), (6) number of nucleotides in one bulge in mature
783 region (≤8), (7) number of biased errors in one bulge in mature region (≤4), (8) number of biased bulges
784 in mature region (≤2), (9) number of errors in mature region (≤7), (10) number of base pairs in the mature
785 region of the predicted hairpin (≥12), (11) percent of mature region in stem (≥80).
786
787 **RNA sequencing.** The Genomic and RNA Profiling Core at Baylor College of Medicine first conducted
788 Sample Quality checks using the NanoDrop spectrophotometer and Agilent Bioanalyzer 2100. We then
789 used Illumina TruSeq Stranded Total RNA library preparation protocol (p/n 15031048, revE, document
790 #RS-122-9007) along with ThermoFisher's ERCC RNA Spike-In Control Mixes Protocol (publication
791 number 4455352, rev. D). Our process is as follows:
792 *Illumina TruSeq stranded total RNA sample preparation protocol*: Total RNA samples were

793 normalized to 250ng each, based on picogreen quantitation, and ERCC RNA Spike-In Controls (p/n
794 4456739) were incorporated into each sample. Using the TruSeq Stranded Total RNA Library Prep Gold
795 Kit (p/n RS-122-2301), samples then underwent ribosomal RNA reduction and subsequently fragmented
796 and primed with random hexamers to produce first strand cDNA. During second strand cDNA synthesis,
797 RNA templates were removed and replaced with cDNA strands containing dUTP. The ds-cDNA was then
798 purified using Beckman Coulter AMPure XP beads (p/n A63881).
799 *Library preparation:* Libraries were created from the cDNA by attaching an adenosine to the 3' end
800 and ligating unique adapters to the ends (for more information on this process, see below). The ligated
801 products underwent 15 cycles of amplification and a final bead purification. The resulting libraries were
802 quantitated using the NanoDrop spectrophotometer and fragment size assessed using the Agilent 2100
803 Bioanalyzer. A qPCR assay was performed on the libraries to determine the concentration of adapter
804 ligated fragments using the Applied Biosystems ViiA 7 Quantitative PCR instrument and a KAPA
805 Library Quant Kit (p/n KK4824). All samples were pooled equimolarly and re-quantitated by qPCR, and
806 also re-assessed on the Bioanalyzer.
807 *Cluster generation by bridge amplification: HiSeq 2500 HOM.* Using the concentration from the
808 ViiA7 qPCR machine above, 26pM of equimolarly pooled library was loaded onto three lanes of a high
809 output v4 flowcell (Illumina p/n PE-401-4001) and amplified by bridge amplification using the Illumina
810 cBot machine (cBot protocol: PE_HiSeq_Cluster_Kit_v4_cBot_recipe_v9.0). PhiX Control v3 adapter-
811 ligated library (Illumina p/n FC-110-3001) is spiked-in at 2% by weight to ensure balanced diversity and
812 to monitor clustering and sequencing performance. A paired-end 100 cycle run was used to sequence the
813 flowcell on a HiSeq 2500 Sequencing System (Illumina p/n FC-401-4003). An average of 129 million
814 read pairs per sample was sequenced.
815 *End repair* converts the overhangs caused by fragmentation into blunt or polished ends. The 3' to 5'
816 exonuclease activity of the End Repair mix removes the 3' overhangs, and polymerase activity fills in the
817 5' overhangs.
818 *Adenylation*: a single 'A' nucleotide is added to the 3' ends of the blunt fragments.
819 *Adapter ligation*: an adapter is ligated to the 3' end of the DNA fragment with a corresponding 'T'
820 nucleotide.
821 *Absolute expression*: The absolute gene expression was calculated as DESeq2-normalized counts as
822 previously described (Love *et al.*, 2014) (**Table S7**).
823 *Samples*: RNAseq was performed in triplicate from whole C57BL/6J mouse brains at 3 weeks of age.
824
825 **Gene Set Enrichment Analysis (GSEA).** GSEA was performed as previously described (Subramanian *et*

826 *al.*, 2005). The cumulative distribution function was conducted by performing 1000 random gene-set
827 membership assignments. A nominal p-value < 0.01 and an FDR < 0.25 were used to assess the
828 significance of the enrichment score (ES). HITS-CLIP data were obtained from the literature and were
829 initially acquired as follows: Pum1 and Pum2 from neonatal murine brains (Zhang *et al.*, 2017), Fmrp
830 from cerebellum, cortex, and hippocampus together (Maurin *et al.*, 2018), Ago2 from neocortex at
831 embryonic day 13 (Chi *et al.*, 2009), Rbfox3 from mouse brain (age not specified) (Weyn-Vanhentenryck
832 *et al.*, 2014), Nova from mouse brain (age not specified) (Zhang *et al.*, 2010), Ptpb2 from neocortex at
833 embryonic day 18.5 (Licatalosi *et al.*, 2012), Mbnl2 from hippocampus at 8-12 weeks of age (Charizanis
834 *et al.*, 2012), and Apc from mouse brain at embryonic day 14 (Preitner *et al.*, 2014). For consistency all
835 the HITS-CLIP data were ranked according to their RPKM.
836 For the normalized RPKM-GSEA analysis we performed RNAseq experiments (as described above),
837 in triplicate, from WT C57BL/6 mouse brain at 3 weeks of age (we chose this age to be comparable to the
838 other HITS-CLIP datasets) to infer the basal level of gene expression by DESeq2-normalized counts (see
839 above). We then normalized the RPKM values by the DESeq2-normalized counts and repeated the GSEA
840 enrichment analysis.
841
842 **Gene ontology analyses.** All gene ontology analyses were performed with David Gene Ontology (GO)
843 and only categories with FDR<0.05 were considered. David GO for the Pum1 interactome considered the
844 entire interactome as background. For GSEA HITS-CLIP targets shared among Pum1, Pum2, Fmrp,
845 Ago2, and Rbfox3, we considered the entire set of all targetomes together as background.
846
847 **Myc and GST cloning procedure with in vitro immunoprecipitation (IP) assays.** Human *PUM1* full-
848 length cDNA was amplified by PCR and subcloned in a pRK5 plasmid containing the Myc tag sequence
849 (Addgene, pRK5-Myc-Parkin #17612) at the N-terminal by using SalI (New England Biolabs, # R3138S)
850 and NotI (New England Biolabs, #R0189S) restriction enzymes to replace *Parkin* with *PUM1*. For GST,
851 the human full-length *PUM1* cDNA was, again, subcloned first in the pRK5 plasmid containing the GST
852 tag sequence (Addgene, pRK5-HA GST RagC wt, #19304) at the N-terminal by using SalI and NotI
853 restriction enzymes to replace *RagC* with *PUM1*. Human *FMRP*, *AGO2* and *CNOT1*, full-length cDNA
854 were cloned and contain the GST tag sequence at the N-terminal as described for GST-*PUM1*.
855 To introduce the T1035S or R1147W mutations we used the QuikChange II XL Multi Site-Directed
856 Mutagenesis kit (Agilent Technologies, #200521). The primers for the single mutagenesis experiments
857 were designed by QuikChange software (Stratagene, San Diego, https://www.genomics.agilent.com/
858 primerDesignProgram.jsp).

859 For IP, HEK293T cells were seeded in 6-well plates for 24 h and then transfected with 250 ng of
860 either WT or mutant PUM1 plasmid with one of the interactors using the jetPRIME Transfection Reagent
861 (Polyplus transfection, #55-132) as per the manufacturer's protocol. pRK5-Myc empty plasmid (no
862 cDNA) was used as a negative control. After 48 h, the cells were collected and processed for
863 immunoprecipitation. Protein lysates were incubated overnight at 4°C with mouse α-Myc antibody
864 (1:400, [Cell Signaling Technologies, #2276]) on a rotisserie tube rotator. The next day, the beads were
865 washed four times with an IP lysis buffer and resuspended in 40 μL elution buffer (lysis buffer, NuPAGE
866 10X Reducing Agent [Invitrogen, #NP0009], NuPAGE LDS sample buffer 4X [Invitrogen, #NP0007])
867 and boiled at 95°C for 10 minutes before loading the samples in NuPAGE 4%–12% Bis-Tris Gels
868 (Invitrogen, #NP0335BOX & #NP0336BOX) for further resolution and western blot analysis. Antibodies:
869 mouse α-Myc antibody [1:2000, (Cell Signaling Technologies, #2276)], rabbit α-GST antibody [1:1000,
870 (Cell Signaling Technologies, #2625)], mouse α-GAPDH [1:10000, (Millipore, #CB1001)].
871
872 **Primers.** For the qPCR analysis to unambiguously distinguish spliced cDNA from genomic DNA
873 contamination, specific exon primers were designed to amplify across introns of the gene tested. The
874 primers for all genes tested were designed with Primer3 (Koressaar & Remm, 2007; Untergasser *et al*,
875 2012). Cloning primers were manually designed to amplify the longest spliced gene isoform tested; if
876 there was more than one isoform according to the UCSC Genome Browser (https://genome.ucsc.edu/), we
877 chose the longest. See **Supplementary Table 8** for primer sequences.
878
879 **Quantification and Statistical Analysis**
880 **Experimental design**
881 For protein and RNA quantification from patient-derived cell lines, we used values from at least six
882 independent experiments with three biological replicates for each experiment. At every stage of the study,
883 the experimenter was blinded to the identity of control and patient-derived cell lines. For example, for the
884 data regarding both human patient-derived cell lines and mice, Experimenter #1 made a list of samples
885 and controls to be tested, and Experimenter #2 randomized this list and re-labeled the tubes; Experimenter
886 #2 was the only person with the key to identify the samples. These samples were then distributed to
887 Experimenter #3 to culture the cells, then to Experimenter #1 to perform western blots and qRT-PCR, and
888 lastly Experimenters #1 and #4 analyzed the data. Only then was the key applied to identify the samples.
889 For mouse experiments, the experimenters were randomized and blinded as described above. The number
890 of animals used and sex, and the specific statistical tests used, are indicated for each experiment in the
891 figure legends. Sample size was based on previous experience using the same mice (Gennarino *et al.*,

892 2015).
893
894 **Software and statistical analysis.** Statistical significance was analyzed using GraphPad Prism 8
895 (https://www.graphpad.com/ scientific-software/prism/) and Excel Software (Microsoft). All data are
896 presented as mean ± SEM. Statistical details for each experiment can be found in the figures and the
897 legends. The range of expression levels in qPCR was determined from at least six independent
898 experiments with three biological replicates by calculating the standard deviation of the **Δ**Ct (Pfaffl,
899 2001). The range of expression levels in western blots was determined from at least six independent
900 experiments with at least six biological replicates. P values were calculated by Student's T-test or analysis
901 of variance with Tukey's post hoc analysis. For the IP and protein quantification in patient cell lines in
902 **Figure 7**, we had only one PADDAS patient, so the six repeated experiments were technical replicates
903 rather than biological replicates. We therefore calculated the statistical significance based on these
904 technical replicates in comparison to the three biological replicates (i.e., healthy controls).
905
906 **Data Availability**
907 **Materials and reagents**
908 Further information and requests for resources, reagents, and mouse models used in this manuscript
909 should be directed to and will be fulfilled by Vincenzo A. Gennarino (vag2138@cumc.columbia.edu).
910
911 **Code and raw data**
912 No software was generated for this project. All software used in this study is publicly available and links
913 are provided as appropriate in different sections of the Materials and Methods. Mass spectrometry, RNA
914 sequencing and microRNA sequencing raw data generated during this study are available at PRIDE
915 Archive at https://www.ebi.ac.uk/pride/archive, and Gene Expression Omnibus (GEO) at
916 https://www.ncbi.nlm.nih.gov/geo/ with the accession numbers pending.
917
918

919 **Main figure titles and legends**

920 **Figure 1. A brain-specific Pum1 interactome.** (**A**) Network of putative Pum1 interactors in 10-week-
921 old mouse brain (circles connected to Pum1 by gray lines). Interactions between interactors (purple lines)
922 inferred by g:GOSt from Corum and the Human Protein Atlas (see Materials and Methods). The proteins
923 in each of the 22 clusters are listed to the right. All putative Pum1 interactors are available in
924 **Supplementary Table 1**. (**B**) Bubble plots show the top categories from gene ontology analyses of Pum1
925 interactors from whole brain, hippocampus, cortex, and cerebellum. Only the categories with fold
926 enrichment >1.5 and FDR<0.05 are shown; not all are labeled because of space limitations. The full list of
927 gene ontology categories are available in **Supplementary Table 2**.

928

929 **Figure 2. Validation of Pum1 associations with post-transcriptional RNA-binding proteins in mouse**
930 **brain.** (**A**) Representative western blot of proteins pulled down by IP against Pum1 compared to IgG
931 from wild-type mice brain without (*left*) and with (*right*) RNase treatment. In this panel, after IP-Pum1,
932 we immunoblotted for Pum1 (positive control), Pum2, Fmrp, Ago2, Rbfox3, Cnot1, and Mov10. (See
933 Materials and Methods.) (**B**) Representative western blot of the reciprocal IPs against Pum2, Fmrp, Ago2,
934 Rbfox3, Cnot1 or Mov10. Each IP was immunoblotted against Pum1 and the putative interactor. (**C**)
935 Representative western blots of the same proteins validated in panels **A** and **B** after IP against PUM1 with
936 or without RNase treatment from HEK293T cell lines. In panels **A** through **C**, IP against IgG was used as
937 a negative control and Input (1% from the initial protein lysate) as a loading control. The numbers on the
938 right are the respective molecular weights expressed in kilodaltons (kDa). All the experiments were
939 repeated at least six times. All mice were sacrificed at 10 weeks of age. See **Figure 2–source data 1** for
940 the original blots.

941

942 **Figure 3. Effects of Pum1 loss on interactions among the six RNA-binding proteins.** Representative
943 western blot of the proteins pulled down by (**A**) Pum2, (**B**) Fmrp, (**C**) Rbfox3, (**D**) Mov10, (**E**) Ago2, and
944 (**F**) Cnot1 from WT and *Pum1*$^{-/-}$ mouse brain at 10 weeks of age. IP against IgG was used as a negative
945 control, and Input (1% from the initial protein lysate) as a loading control. Molecular weights to the right
946 are expressed in kilodaltons (kDa). All the experiments were repeated at least four times. Since Rbfox3
947 and Mov10 interactions with Pum1 are RNA-dependent we did not perform IP from *Pum1*$^{-/-}$ mouse brain.
948 See **Figure 3–source data 1** for the original blots.

949

950 **Figure 4. Pum1 interactors and the microRNA machinery show brain region- and sex-specific**
951 **responses to Pum1 loss.** Representative western blots of Pum1, Pum2, Fmrp, Ago2, Rbfox3, Cnot1, and

952 Mov10 in (**A**) cerebellum, (**B**) hippocampus, and (**C**) cortex in both male (left panel) and female (right
953 panel) WT, *Pum1*$^{+/-}$, and *Pum1*$^{-/-}$ mice. The same number of males and females at 10 weeks of age was
954 used for a total of at least 18 mice per genotype. Graphs below show quantification for each protein by
955 brain region, sex, and genotype. All data were normalized to Gapdh protein levels. All experiments were
956 performed at least 9 times per genotype from mice at 10 weeks of age (data represent mean ± SEM). *P*
957 values were calculated by two-tailed Student's t test. $*p < 0.05$, $**p < 0.01$, $***p < 0.001$. See **Figure 4–**
958 **figure supplement 2A** for mRNA quantification for each interactor, brain region, and sex. P1 indicates
959 Pumilio1. See **Figure 4–Source data 1** for all western blot quantifications. (**D**) Heatmap showing 166
960 microRNAs from mouse cerebellum in *Pum1*$^{-/-}$ male and female mice at 10 weeks of age that were
961 dysregulated (fold change -3 to +3) relative to wild-type cerebellum. Three cerebella per genotype and
962 sex were analyzed. The full list of miRNA names and fold changes are available in **Supplementary**
963 **Table 3**. (**E**) Heatmap showing mRNA quantification by qPCR for 49 targets co-bound by a minimum of
964 eight dysregulated miRNAs (>20% change) from panel **D**. Three cerebella per genotype and sex were
965 analyzed. Statistical significance and magnitude of dysregulation are illustrated for both male and female
966 in **Figure 4–figure supplement 2B**. The entire list of targets predicted to be co-bound by at least two
967 miRNAs are reported in **Supplementary Table 4**. See **Figure 4–source data 1** and **2** for the original
968 blots and quantifications.
969
970 **Figure 5. Pum1 and its RNA-binding protein interactors share many neuronal mRNA targets.** (**A**)
971 Enrichment plots generated by Gene Set Enrichment Analysis (GSEA) of Pum1, Pum2, Rbfox3, and
972 Ago2 HITS-CLIP targets plotted again Fmrp HITS-CLIP data ranked by RPKM. Pum1, Pum2, Rbfox3,
973 and Ago2 targets are enriched at the top 10th percentile of the Fmrp targets with FDR=0. (**B**) GSEA
974 analysis scores of HITS-CLIP data from each negative control (Apc, Nova, Ptpb2, and Mbnl2) plotted
975 against Fmrp HITS-CLIP data ranked by RPKM. The negative controls have a maximum enrichment
976 score of 0.36 for Apc ranking at the top 44.7% with FDR=1. (**C**) GSEA analysis scores of Pum1, Pum2,
977 Rbfox3, and Ago2 HITS-CLIP data plotted against Fmrp HITS-CLIP data divided into 10-percentile bins
978 and ranked by RPKM shows the shared targets are among the top percentiles of targets for each protein.
979 (**D**) GSEA analysis scores of the HITS-CLIP data for Fmrp, Pum2, Ago2, Rbfox3 and four negative
980 controls (Apc, Nova, Ptpb2, and Mbnl2) against Pum1 HITS-CLIP data ranked by RPKM. The targets of
981 Fmrp, Ago2, Pum2, and Rbfox3 are enriched at the top 5th to 18th percentile of Pum1 targets. (**E**) GSEA
982 analysis of the shared targets between Pum1, Pum2, Ago2, and Rbfox3 against Fmrp showing that they
983 are enriched in the top 5th percentile of Fmrp targets ranked by RPKM. (**F**) Pum1, Pum2, Ago2, and
984 Rbfox3 shared targets plotted against Fmrp HITS-CLIP targets ranked by RPKM and divided into 10-

985 percentile bins shows that all of their respective targets are enriched at the top 10th percentile of the Fmrp
986 targets ranked by RPKM. (**G**) GSEA analysis scores of the targets shared by Pum1, Pum2, Ago2, and
987 Rbfox3 and the four negative controls (Apc, Nova, Ptpb2, and Mbnl2) plotted against Fmrp. At best the
988 negative controls are enriched at the top 40% with a maximum ES of 0.41. For all the GSEA analyses, the
989 False Discovery Rate (FDR) was provided by GSEA: **FDR<0.05 and ***FDR<0.01. ES=Enrichment
990 score (blue line). Note that lowest rank at max percentage indicates stronger targets in the rank (see
991 Materials and Methods). The full list of shared targets is reported in **Supplementary Table 5**.
992
993 **Figure 6. The R1147W mutation, but not T1035S, destabilizes PUM1 interactors.** (**A**) IP
994 against PUM1 from PADDAS (R1147W) patient (Subject 1 or S1)-derived fibroblasts confirms
995 the interactions between PUM1 (used here as a positive control), and PUM2, FMRP, AGO2,
996 CNOT1, and MOV10. *Bottom panel*: protein quantification shows loss of interaction between
997 PUM1-R1147W and AGO2, CNOT1 and MOV10 compared to three age- and sex- matched
998 control fibroblasts. Input (1%) was used as a loading control and IP against IgG was used as a
999 negative control. (**B**) IP against PUM1 from two PRCA (T1035S) patient (S2 and S3)-derived
1000 lymphoblastoid cell lines confirm the interaction between PUM1 (used here as positive control),
1001 and PUM2, FMRP, AGO2, CNOT1, and MOV10. *Bottom panel*: protein quantification shows a
1002 slight decrease in interactions with FMRP and AGO2, and a slight increase with CNOT1 and
1003 MOV10, compared to age- and sex- matched lymphoblastoid controls. Input (1%) was used as a
1004 loading control and IP against IgG was used as a negative control. In **A** and **B**, the amount of
1005 protein pulled down compared to IP-PUM1 was quantified as follows: [IP^X/($Input^X$/$GAPDH^X$)]/
1006 [IP^{PUM1}/($Input^{PUM1}$/$GAPDH^{PUM1}$)], where X is the protein of interest. (**C**) Representative western
1007 blots (*left panels*) and relative quantification (*bar graphs to the right*) of protein levels for
1008 PUM1, PUM2, FMRP, AGO2, CNOT1, and MOV10 in PADDAS patient-derived fibroblasts
1009 and PRCA patient-derived lymphoblastoid cells compared to their respective age- and sex-
1010 matched fibroblast (for PADDAS patients) and lymphoblastoid (for PRCA patients) controls.
1011 Data were normalized to Gapdh protein levels. From **A** to **C**, all the experiments were performed
1012 at least six times. Data represent mean ± SEM. P values were calculated by two-tailed Student's t
1013 test. *$p < 0.05$, **$p < 0.01$, ***$p < 0.001$. See **Figure 6–source data 1** for the original blots.
1014
1015 **Figure 7. RBP complexes with PUM1 R1147W are destabilized *in vitro* and shared neuronal targets**

1016 **are upregulated only in PADDAS.** (**A**-**D**) Representative western blots and relative IP quantification
1017 (*bar graphs*) of IP against Myc-PUM1-WT, Myc-PUM1-T1035S (PRCA), or Myc-PUM1-R1147W
1018 (PADDAS) followed by immunoblotting for: (**A**) GST-AGO2, (**B**) GST-CNOT1, (**C**) GST-FMRP, and
1019 (**D**) GST-PUM1-WT. Myc- and GST-tagged proteins were co-transfected in HEK293T cells in equal
1020 quantities (250ng each). The molecular weights were expressed in kilodaltons (kDa). The amount of
1021 protein pulled down compared to IP-PUM1 was quantified as $[IP^{X}/(Input^{X}/GAPDH^{X})]/$
1022 $[IP^{PUM1}/(Input^{PUM1}/ GAPDH^{PUM1})]$, where X is the protein of interest. (**E**) qPCR analysis of validated
1023 PUM1-specific targets from PADDAS patient-derived fibroblasts (S1, blue bars) compared to three age-
1024 and sex-matched fibroblast control cell lines, and PRCA patient-derived lymphoblastoid cell lines (S2 and
1025 S3, orange bars) compared to the three age- and sex-matched lymphoblastoid control cell lines. (**F**)
1026 mRNA level quantification of PUM1 neuronal targets in common with FMRP, PUM2, AGO2, and
1027 RBFOX3 (**Figure 5E** and **Supplementary Table 5**) in fibroblasts from subject 1 (PADDAS patient,
1028 R1147W) compared to the three age- and sex-matched control fibroblast lines (blue bars), and in
1029 lymphoblastoid cells from subjects 2 and 3 (PRCA patients, T1035S) compared to the three age- and sex-
1030 matched control lymphoblastoid cell lines (orange bars). For **E** and **F**, all data were normalized to
1031 *GAPDH* mRNA levels and experiments performed at least three times. Only genes expressed in both
1032 fibroblasts and lymphoblasts are represented here for a total of 10 for panel **E** and 55 for panel **F**. Data
1033 represent mean ± SEM. P values were calculated by two-tailed Student's t test. $*p < 0.05$, $**p < 0.01$,
1034 $***p < 0.001$. The full list of shared targets expressed in fibroblast and lymphoblast cell lines is reported
1035 in **Supplementary Table 5. See Figure 7–source data 1 for the original blots.**
1036
1037 **Supplemental figure titles and legends**
1038 **Figure 1–figure supplement 1. Immunoprecipitation (IP) antibody specificity against Pum1 from**
1039 **mouse brain and Pum1 interactor validation.** (**A**) Pre-IP, IP, and post-IP against Pum1 and IgG from
1040 wild-type mouse brain show the specificity of the antibody used against Pum1. Pre-IP represents 1% from
1041 the initial protein lysate as a loading control while 10% of the protein lysate after IP-Pum1 was loaded as
1042 post-IP. The numbers on the right show molecular weight in kilodaltons (kDa). (**B**) Principal component
1043 analysis (PCA) of IP-Pum1 followed by mass spectrometry (MS) in WT adult mouse brains compared
1044 with IP against IgG; each dot represents two combined samples for a total of 6 samples processed by mass
1045 spectrometry. (**C**) Representative western blot of Rptor, Cad, Anapc1 and Fzr1 proteins pulled down by
1046 IP against Pum1 (used here as positive control) from WT mice. (**D**) Representative western blot of the
1047 reciprocal co-Ips against Anapc1, Fzr1, Rptor, and Cad. Each co-IP was immunoblotted against Pum1 and
1048 the pulled down protein used here as a reference protein to confirm the respective protein-protein

1049 interaction. For **C** and **D**, IP against IgG was used as a negative control, and Input (1% from the initial
1050 protein lysate) as a loading control. Molecular weights are expressed in kilodaltons (kDa) to the right. All
1051 the experiments were repeated at least four times. All mice were sacrificed at 10 weeks of age with an
1052 equal number or male and female. See **Figure 1–figure supplement 1–source data 1** for the original
1053 blots.

1054 **Figure 1–figure supplement 2. Pum1 interactors differ by brain region.** (**A**) Principal component
1055 analysis (PCA) of IP-Pum1 followed by mass spectrometry (MS) in cortex, hippocampus, and cerebellum
1056 from WT mice. IP against IgG was used as a negative control. Each dot represents a total of 3 samples
1057 processed by MS for each brain region. (**B**) Pum1 interactome from cerebellum, hippocampus, cortex and
1058 the rest of the brain (i.e., excluding those three regions) showing all Pum1 putative interactors with a fold
1059 change > 1.5 (see also **Supplementary Table 1**), for a total of 1,500 proteins. Node colors represent
1060 different brain regions or the overlap between two or more brain regions as noted. (**C**) After IP against
1061 Pum1 we immunoblotted for Pum1 (positive control), Anapc1, Cnot1 and Pum2. While Cnot1 and
1062 Anapc1 can be pulled down from all three brain regions, Pum2 can only be pulled down from cortex. For
1063 **A-C** we combined cerebellar and cortical tissues from eight wild-type mice (4 male and 4 female) for a
1064 total of 24 mice in triplicate for cerebellum and cortex, while for hippocampus we combined tissues from
1065 ten wild-type mice (5 female and 5 male) for a total of 30 mice in triplicate. All mice were 10 weeks of
1066 age. IP against IgG was used as a negative control. Molecular protein weights are expressed in kilodaltons
1067 (kDa). (**D-F**) The three most enriched protein complexes among the Pum1 interactors for each brain
1068 region are shown in (**D**) for the anaphase promoting complex/cyclosome (APC/C); (**E**) for the mTOR
1069 pathway; (**F**) for RNA-silencing (RISC), CCR4-NOT, translation initiation and polyA binding. Edge
1070 colors (**D**, **E**, and **F**) represent a specific brain region: red for cortex, green for cerebellum, blue for
1071 hippocampus, and gray for proteins in common between two or more brain regions. (**G**) Western blot
1072 analysis at 10 weeks of age to evaluate Pum2 expression levels in eight different brain regions as well as
1073 whole brain. Pum2 is highly expressed in olfactory bulbs and amygdala, and expressed at similar levels in
1074 hippocampus, cerebellum, and cortex. HP: hippocampus; CB: cerebellum; CX: cortex; MB: midbrain;
1075 OB: olfactory bulbs; AM: amygdala; SN: substantia nigra pars compacta; BS: brain stem; WB: whole
1076 brain. See **Figure 1–figure supplement 2–source data 1** for the original blots.

1077 **Figure 2–figure supplement 1. Immunoprecipitation (IP) against Pum1 from whole brain in *Pum1*$^{-/-}$**
1078 **mice.** IP against Pum1 in *Pum1*$^{-/-}$ mouse demonstrates the complete absence of Pum1 and thus the
1079 specificity of the anti-Pum1 antibody. IP against IgG was used as a negative control, and Input (1% from
1080 the initial protein lysate) as a loading control. Molecular weights at the right are in kilodaltons (kDa). All

1081 the experiments were repeated at least four times. IP against IgG was used as a negative control, and Input
1082 (1% from the initial protein lysate) as a loading control. Equal numbers of male and female mice were
1083 sacrificed at 10 weeks of age. See **Figure 2–figure supplement 1–source data 1** for the original blots.

1084 **Figure 3–figure supplement 1. Immunoprecipitation (IP) against Pum1 interactors from whole**
1085 **brain in wild-type and *Pum1*$^{-/-}$ mice with and without RNase treatment.** (**A-F**) Representative western
1086 blot of the proteins pulled down by (**A**) Pum2, (**B**) Fmrp, (**C**) Ago2, (**D**) Cnot1, (**E**) Mov10, and (**F**)
1087 Rbfox3 from wild-type (WT, *left panel*) and *Pum1*$^{-/-}$ (*right panel*) mouse brain without (*left panel*) and
1088 with (*right panel*) RNase treatment. IP against IgG was used as a negative control, and Input (1% from
1089 the initial protein lysate) as a loading control. Molecular weights at the right are in kilodaltons (kDa). All
1090 the experiments were repeated at least four times. IP against IgG was used as a negative control, and Input
1091 (1% from the initial protein lysate) as a loading control. Equal numbers of male and female mice were
1092 sacrificed at 10 weeks of age. See **Figure 3–figure supplement 1–source data 1** for the original blots.

1093 **Figure 4–figure supplement 1. Protein and mRNA quantification from whole brain in WT, *Pum1*$^{+/-}$**
1094 **and *Pum1*$^{-/-}$ mice.** (**A**) Representative western blot with relative quantifications of Pum1, Pum2, Fmrp,
1095 Ago2, Rbfox3, Cnot1, and Mov10 from the whole brain in WT, *Pum1*$^{+/-}$ and *Pum1*$^{-/-}$ mice. All data were
1096 normalized to Gapdh protein levels. The numbers on the right are the respective molecular weights
1097 expressed in kilodaltons (kDa). (**B**) mRNA level quantification by qPCR of *Pum1*, *Pum2*, *Fmrp*, *Ago2*,
1098 *Rbfox3*, *Cnot1*, and *Mov10* from whole brain in WT, *Pum1*$^{+/-}$ and *Pum1*$^{-/-}$ mice. Again, all data were
1099 normalized to *Gapdh* mRNA levels. All the experiments were conducted with equal number of male (at
1100 least 6 per genotype) and female (at least 6 per genotype) mice at 10 weeks of age, for a total of at least
1101 12 mice per genotype, performed at least six times per genotype (data represent mean ± SEM). The p
1102 values were calculated by the Student's t test. *$p < 0.05$, **$p < 0.01$, ***$p < 0.001$. See **Figure 4–figure**
1103 **supplement 1–source data 1** for the original blots.

1104 **Figure 4–figure supplement 2. mRNA quantification of Pum1 interactors by brain region and sex**
1105 **and the 49 targets co-bound by at least eight dysregulated miRNAs in mouse cerebellum.** (**A**)
1106 mRNA levels in cerebellum, hippocampus, and cortex in male and female for all the validated Pum1
1107 interactors. The same number of mice were used here as in **Figure 4A-C** for a total of at least 9 mice per
1108 genotype and sex at 10 weeks of age. All data were normalized to *Gapdh* mRNA levels. All the
1109 experiments were performed at least six times (data represent mean ± SEM). (**B**) qPCR in cerebellum of
1110 male (*left*) and female (*right*) mice at 10 weeks of age for the 49 targets co-bound by at least eight
1111 dysregulated miRNAs (with minimum 20% change in expression) from **Figure 4E** and **Supplementary**

1112 **Table 4**. All the experiments were performed in triplicate for three different biological replicates for both
1113 male and female (data represent mean ± SEM). The *p* values were calculated by two-tailed Student's t
1114 test. *$p < 0.05$, **$p < 0.01$, ***$p < 0.001$.

1115 **Figure 5–figure supplement 1. Pum1, Pum2, Ago2, Fmrp, and Rbfox3 share a number of targets in**
1116 **the mouse brain.** (**A**) Gene Set Enrichment Analysis (GSEA) of Pum1 HITS-CLIP data plotted against
1117 HITS-CLIP data from the negative controls (RNA binding proteins that did not show up in the Pum1
1118 interactome: Ptpb2, Nova, Apc, and Mbnl2) reveals no significant enrichment. (**B**-**C**) Gene ontology
1119 analysis of the HITS-CLIP targets shared between Pum1, Pum2, Fmrp, Ago2, and Rbfox3 reveals
1120 enrichment for certain (**B**) biological functions and (**C**) cellular localization. Only categories with
1121 FDR<0.05 and fold enrichment > 5 were plotted in **B** and **C**. (**D**) Venn diagram of miRNAs identified by
1122 Pum1, and Pum2 shows almost 100% overlap with the miRNAs pulled down by Fmrp HITS-CLIP. The
1123 full list of shared miRNAs is reported in **Supplementary Table 6**. (**E**) GSEA of HITS-CLIP data
1124 normalized against gene expression in mouse brain at 3 weeks of age (see Materials and Methods) of
1125 Pum1, Pum2, Rbfox3, and Ago2 against Fmrp HITS-CLIP data ranked by normalized RPKM. (**F**) GSEA
1126 of HITS-CLIP data normalized against gene expression in mouse brain at 3 weeks of age (see Materials
1127 and Methods) of Mbnl2, Apc, Nova, and Ptpb2 plotted against Fmrp HITS-CLIP data ranked by
1128 normalized RPKM. Mbnl2, Ptpb2, Apc, and Nova were used as negative controls. (**G**) Fmrp, Pum2,
1129 Ago2, Rbfox3 shared targets, and targets of the four negative controls, plotted against Pum1 HITS-CLIP
1130 data ranked by normalized RPKM. (**H**) Pum1, Pum2, Ago2, Rbfox3 shared targets plotted against Fmrp
1131 HITS-CLIP data ranked by normalized RPKM. The RNAseq gene expression changes are reported in
1132 **Supplementary Table 7**. For all GSEA analyses the False Discovery Rate (FDR) was provided by
1133 GSEA, ***FDR < 0.01. ES=Enrichment score (blue line). Note that lowest rank at max percentage ES
1134 indicates stronger targets in the rank.

1135 **Figure 6–figure supplement 1. PUM1 validation experiments in patient-derived cells.** (**A**-**B**) Pre-IP,
1136 IP, and post-IP against PUM1 and IgG from (**A**) PADDAS fibroblasts and (**B**) PRCA lymphoblastoid
1137 cells. In both cell lines we were able to pull down 100% of PUM1. Pre-IP represents 1% from the initial
1138 protein lysate as a loading control, while 10% of the protein lysate was loaded as post-IP. Molecular
1139 weights provided at right in kilodaltons (kDa). (**C**) mRNA level quantification for all of the
1140 immunoblotted proteins in **Figure 6C** in PADDAS and PRCA patient-derived cell lines compared to their
1141 respective age-, sex-, and cell-type-matched controls. All data were normalized to *GAPDH* mRNA levels,
1142 and experiments performed at least six times. Data represent mean ± SEM. See **Figure 6–figure**
1143 **supplement 1–source data 1** for the original blots.

1144 **Figure 7–figure supplement 1. PUM1 validation experiments *in vitro*.** (**A-D**) Representative western
1145 blots (upper panel) and relative IP quantification (bottom panel) of IP against Myc-PUM1-WT, Myc-
1146 PUM1-T1035S (PRCA), or Myc-PUM1-R1147W (PADDAS) followed by immunoblotting for: (**A**) GST-
1147 PABPC1, (**B**) GST-PABPC4, (**C**) GST-EIF4A3, and (**D**) GST-EIF4G3. Myc- and GST-tagged proteins
1148 were co-transfected in HEK293T cells in equal quantities (250ng each). The molecular weights were
1149 expressed in kilodaltons (kDa). The amount of protein pulled down compared to IP-PUM1 was quantified
1150 as $[IP^{X}/(Input^{X}/GAPDH^{X})]/ [IP^{PUM1}/(Input^{PUM1}/GAPDH^{PUM1})]$, where X is the protein of interest.
1151 (**E**) PUM1 half-life in HEK293T at different time points, from zero (cycloheximide treatment) to 5h total
1152 upon transfection of Myc-PUM1-WT, Myc-PUM1-T1035S, or Myc-PUM1-R1147W. The half-life of the
1153 R1147W mutant is significantly shorter than that of WT and T1035S. All data were normalized to
1154 GAPDH and compared to time zero. The experiments were performed at least four times and the data
1155 represent mean ± SEM. The *p* values were calculated by two-tailed Student's t test. $^{**}p < 0.01$, $^{***}p <$
1156 0.001. (**F**) Representative western blots of IP with RNase treatment against Myc-PUM1-WT, Myc-
1157 PUM1-T1035S (PRCA), or Myc-PUM1-R1147W (PADDAS) followed by immunoblotting to
1158 test binding between PUM1 proteins without the RNA. The numbers on the right are the respective
1159 molecular weights expressed in kilodaltons (kDa). See **Figure 7–figure supplement 1–source data 1** for
1160 the original blots.

1161 **Supplementary table titles and legends**

1162 **Supplementary Table 1. Pum1 mass spectrometry results from whole brain and three separate**
1163 **brain regions in 10-week-old mice.** All the proteins have an FDR < 0.05, and only proteins with a Ratio
1164 LFQ-Pum1-WT/LFQ-IgG-WT > 1.5 are reported here.

1165 **Supplementary Table 2. Gene Ontology analysis of Pum1 mass spectrometry from whole brain and**
1166 **the three brain regions.** Only categories with fold enrichment of >1.5 and FDR<0.05 are shown.

1167 **Supplementary Table 3. MicroRNA names and sequences with log2 fold change as represented in**
1168 **Figure 4D.** PC = Predicted Candidate.

1169 **Supplementary Table 4. Predicted target genes for all the differentially expressed miRNA (with at**
1170 **least 25% change) in cerebellum of male and female in wild-type and *Pum1*$^{-/-}$ mice at 10 weeks of**
1171 **age.** The target genes tested to generated Figure 4E and Figure 4–figure supplement 2B have at least 8 co-
1172 bound miRNAs.

1173 **Supplementary Table 5. HITS-CLIP targets common to Pum1, Pum2, Ago2, Rbfox3, and Fmrp.**

1174 **Supplementary Table 6. microRNAs that overlap between Pum1, Pum2, and Fmrp HITS-CLIP**
1175 **data.**

1176 **Supplementary Table 7. RNAseq in mouse brain at 3 weeks of age.**
1177

1178 **Supplementary Table 8. All primer sequences used in this study.**

1179 **References**

1180 Agarwal V, Bell GW, Nam JW, Bartel DP (2015) Predicting effective microRNA target sites in
1181 mammalian mRNAs. *Elife* 4
1182
1183 Almeida A, Bolanos JP, Moreno S (2005) Cdh1/Hct1-APC is essential for the survival of postmitotic
1184 neurons. *The Journal of Neuroscience* 25: 8115-8121
1185
1186 Bah MG, Rodriguez D, Cazeneuve C, Mochel F, Devos D, Suppiej A, Roubertie A, Meunier I, Gitiaux C,
1187 Curie A *et al* (2020) Deciphering the natural history of SCA7 in children. *Eur J Neurol* 27: 2267-2276
1188
1189 Blackinton JG, Keene JD (2014) Post-transcriptional RNA regulons affecting cell cycle and proliferation.
1190 *Semin Cell Dev Biol* 34: 44-54
1191
1192 Blewett NH, Goldstrohm AC (2012) A eukaryotic translation initiation factor 4E-binding protein
1193 promotes mRNA decapping and is required for PUF repression. *Molecular and Cellular Biology* 32:
1194 4181-4194
1195
1196 Bohn JA, Van Etten JL, Schagat TL, Bowman BM, McEachin RC, Freddolino PL, Goldstrohm AC
1197 (2018) Identification of diverse target RNAs that are functionally regulated by human Pumilio proteins.
1198 *Nucleic Acids Research* 46: 362-386
1199
1200 Bonnemason-Carrere P, Morice-Picard F, Pennamen P, Arveiler B, Fergelot P, Goizet C, Hellegouarch
1201 M, Lacombe D, Plaisant C, Raclet V *et al* (2019) PADDAS syndrome associated with hair dysplasia
1202 caused by a de novo missense variant of PUM1. *American Journal of Medical Genetics Part A* 179:
1203 1030-1033
1204
1205 Charizanis K, Lee KY, Batra R, Goodwin M, Zhang C, Yuan Y, Shiue L, Cline M, Scotti MM, Xia G *et*
1206 *al* (2012) Muscleblind-like 2-mediated alternative splicing in the developing brain and dysregulation in
1207 myotonic dystrophy. *Neuron* 75: 437-450
1208
1209 Chartier-Harlin MC, Kachergus J, Roumier C, Mouroux V, Douay X, Lincoln S, Levecque C, Larvor L,
1210 Andrieux J, Hulihan M *et al* (2004) Alpha-synuclein locus duplication as a cause of familial Parkinson's
1211 disease. *Lancet* 364: 1167-1169
1212
1213 Chen D, Zheng W, Lin A, Uyhazi K, Zhao H, Lin H (2012) Pumilio 1 suppresses multiple activators of
1214 p53 to safeguard spermatogenesis. *Current Biology: CB* 22: 420-425
1215
1216 Cheng S, Gallie DR (2007) eIF4G, eIFiso4G, and eIF4B bind the poly(A)-binding protein through
1217 overlapping sites within the RNA recognition motif domains. *The Journal of Biological Chemistry* 282:
1218 25247-25258

1219 Chi SW, Zang JB, Mele A, Darnell RB (2009) Argonaute HITS-CLIP decodes microRNA-mRNA
1220 interaction maps. *Nature* 460: 479-486
1221
1222 Conboy JG (2017) Developmental regulation of RNA processing by Rbfox proteins. *Wiley*
1223 *Interdisciplinary Reviews RNA* 8
1224
1225 Cox J, Mann M (2008) MaxQuant enables high peptide identification rates, individualized p.p.b.-range
1226 mass accuracies and proteome-wide protein quantification. *Nature Biotechnology* 26: 1367-1372

1227
1228 Cox J, Neuhauser N, Michalski A, Scheltema RA, Olsen JV, Mann M (2011) Andromeda: a peptide
1229 search engine integrated into the MaxQuant environment. *J Proteome Res* 10: 1794-1805
1230
1231 Darnell JC, Richter JD (2012) Cytoplasmic RNA-binding proteins and the control of complex brain
1232 function. *Cold Spring Harb Perspect Biol* 4: a012344
1233
1234 Dassi E (2017) Handshakes and fights: the regulatory interplay of RNA-binding proteins. *Front Mol*
1235 *Biosci* 4: 67
1236
1237 De Maio A, Yalamanchili HK, Adamski CJ, Gennarino VA, Liu Z, Qin J, Jung SY, Richman R, Orr H,
1238 Zoghbi HY (2018) RBM17 interacts with U2SURP and CHERP to regulate expression and splicing of
1239 RNA-processing proteins. *Cell Reports* 25: 726-736 e727
1240
1241 Di Grazia A, Marafini I, Pedini G, Di Fusco D, Laudisi F, Dinallo V, Rosina E, Stolfi C, Franze E, Sileri
1242 P *et al* (2021) The Fragile X mental retardation protein regulates RIPK1 and colorectal cancer resistance
1243 to necroptosis. *Cell Mol Gastroenterol Hepatol* 11: 639-658
1244
1245 Dittmann K, Mayer C, Czemmel S, Huber SM, Rodemann HP (2017) New roles for nuclear EGFR in
1246 regulating the stability and translation of mRNAs associated with VEGF signaling. *PloS One* 12:
1247 e0189087
1248
1249 Edwards TA, Pyle SE, Wharton RP, Aggarwal AK (2001) Structure of Pumilio reveals similarity between
1250 RNA and peptide binding motifs. *Cell* 105: 281-289
1251
1252 Enwerem, III, Elrod ND, Chang CT, Lin A, Ji P, Bohn JA, Levdansky Y, Wagner EJ, Valkov E,
1253 Goldstrohm A (2021) Human Pumilio proteins directly bind the CCR4-NOT deadenylase complex to
1254 regulate the transcriptome. *RNA* 27: 445-464.
1255
1256 Friend K, Campbell ZT, Cooke A, Kroll-Conner P, Wickens MP, Kimble J (2012) A conserved PUF-
1257 Ago-eEF1A complex attenuates translation elongation. *Nature Structural & Molecular Biology* 19: 176-
1258 183
1259
1260 Gallie DR (1998) A tale of two termini: a functional interaction between the termini of an mRNA is a
1261 prerequisite for efficient translation initiation. *Gene* 216: 1-11

1262 Gehman LT, Meera P, Stoilov P, Shiue L, O'Brien JE, Meisler MH, Ares M, Jr., Otis TS, Black DL
1263 (2012) The splicing regulator Rbfox2 is required for both cerebellar development and mature motor
1264 function. *Genes & Development* 26: 445-460
1265
1266 Gennarino VA, D'Angelo G, Dharmalingam G, Fernandez S, Russolillo G, Sanges R, Mutarelli M,
1267 Belcastro V, Ballabio A, Verde P *et al* (2012) Identification of microRNA-regulated gene networks by
1268 expression analysis of target genes. *Genome Research* 22: 1163-1172
1269
1270 Gennarino VA, Palmer EE, McDonell LM, Wang L, Adamski CJ, Koire A, See L, Chen CA, Schaaf CP,
1271 Rosenfeld JA *et al* (2018) A mild PUM1 mutation is associated with adult-onset ataxia, whereas
1272 haploinsufficiency causes developmental delay and seizures. *Cell* 172: 924-936 e911
1273

1274 Gennarino VA, Singh RK, White JJ, De Maio A, Han K, Kim JY, Jafar-Nejad P, di Ronza A, Kang H,
1275 Sayegh LS *et al* (2015) Pumilio1 haploinsufficiency leads to SCA1-like neurodegeneration by increasing
1276 wild-type Ataxin1 levels. *Cell* 160: 1087-1098
1277
1278 Gieffers C, Peters BH, Kramer ER, Dotti CG, Peters JM (1999) Expression of the CDH1-associated form
1279 of the anaphase-promoting complex in postmitotic neurons. *PNAS* 96: 11317-11322
1280
1281 Giurgiu M, Reinhard J, Brauner B, Dunger-Kaltenbach I, Fobo G, Frishman G, Montrone C, Ruepp A
1282 (2019) CORUM: the comprehensive resource of mammalian protein complexes-2019. *Nucleic Acids*
1283 *Research* 47: D559-D563
1284
1285 Goldstrohm AC, Hall TMT, McKenney KM (2018) Post-transcriptional regulatory functions of
1286 mammalian pumilio proteins. *Trends in Genetics* 34: 92-990
1287
1288 Hentze MW, Castello A, Schwarzl T, Preiss T (2018) A brave new world of RNA-binding proteins.
1289 *Nature reviews Molecular Cell Biology* 19: 327-341
1290
1291 Humphrey J, Birsa N, Milioto C, McLaughlin M, Ule AM, Robaldo D, Eberle AB, Krauchi R, Bentham
1292 M, Brown AL *et al* (2020) FUS ALS-causative mutations impair FUS autoregulation and splicing factor
1293 networks through intron retention. *Nucleic Acids Research* 48: 6889-6905
1294
1295 Imaizumi T, Mogami Y, Okamoto N, Yamamoto-Shimojima K, Yamamoto T (2019) De novo 1p35.2
1296 microdeletion including PUM1 identified in a patient with sporadic West syndrome. *Congenit Anom*
1297 *(Kyoto)* 59: 193-194
1298
1299 Jin Z, Feng H, Liang J, Jing X, Zhao Q, Zhan L, Shen B, Cheng X, Su L, Qiu W (2020) FGFR3 big up tri,
1300 open7-9 promotes tumor progression via the phosphorylation and destabilization of ten-eleven
1301 translocation-2 in human hepatocellular carcinoma. *Cell Death Dis* 11: 903
1302
1303 Kedde M, van Kouwenhove M, Zwart W, Oude Vrielink JA, Elkon R, Agami R (2010) A Pumilio-
1304 induced RNA structure switch in p27-3' UTR controls miR-221 and miR-222 accessibility. *Nature Cell*
1305 *Biology* 12: 1014-1020
1306
1307 Keene JD (2007a) Biological clocks and the coordination theory of RNA operons and regulons. *Cold*
1308 *Spring Harb Symp Quant Biol* 72: 157-165
1309
1310 Keene JD (2007b) RNA regulons: coordination of post-transcriptional events. *Nature Reviews Genetics* 8:
1311 533-543
1312
1313 Keene JD, Lager PJ (2005) Post-transcriptional operons and regulons co-ordinating gene expression.
1314 *Chromosome Res* 13: 327-337
1315
1316 Kenny PJ, Kim M, Skariah G, Nielsen J, Lannom MC, Ceman S (2020) The FMRP-MOV10 complex: a
1317 translational regulatory switch modulated by G-Quadruplexes. *Nucleic Acids Research* 48: 862-878
1318
1319 Kenny PJ, Zhou H, Kim M, Skariah G, Khetani RS, Drnevich J, Arcila ML, Kosik KS, Ceman S (2014)
1320 MOV10 and FMRP regulate AGO2 association with microRNA recognition elements. *Cell Reports* 9:
1321 1729-1741
1322

1323 Khalil B, Morderer D, Price PL, Liu F, Rossoll W (2018) mRNP assembly, axonal transport, and local
1324 translation in neurodegenerative diseases. *Brain Res* 1693: 75-91
1325
1326 Kim K, Hessl D, Randol JL, Espinal GM, Schneider A, Protic D, Aydin EY, Hagerman RJ, Hagerman PJ
1327 (2019) Association between IQ and FMR1 protein (FMRP) across the spectrum of CGG repeat
1328 expansions. *PloS One* 14: e0226811
1329
1330 Koressaar T, Remm M (2007) Enhancements and modifications of primer design program Primer3.
1331 *Bioinformatics* 23: 1289-1291
1332
1333 Lai KL, Liao YC, Tsai PC, Hsiao CT, Soong BW, Lee YC (2019) Investigating PUM1 mutations in a
1334 Taiwanese cohort with cerebellar ataxia. *Parkinsonism Relat Disord* 66: 220-223
1335
1336 Le H, Tanguay RL, Balasta ML, Wei CC, Browning KS, Metz AM, Goss DJ, Gallie DR (1997)
1337 Translation initiation factors eIF-iso4G and eIF-4B interact with the poly(A)-binding protein and increase
1338 its RNA binding activity. *The Journal of Biological Chemistry* 272: 16247-16255

1339 Lee EJ, Seo E, Kim JW, Nam SA, Lee JY, Jun J, Oh S, Park M, Jho EH, Yoo KH *et al* (2020) TAZ/Wnt-
1340 beta-catenin/c-MYC axis regulates cystogenesis in polycystic kidney disease. *PNAS* 117: 29001-29012
1341
1342 Lee JT, Wheeler TC, Li L, Chin LS (2008) Ubiquitination of alpha-synuclein by Siah-1 promotes alpha-
1343 synuclein aggregation and apoptotic cell death. *Human Molecular Genetics* 17: 906-917
1344
1345 Leeb M, Dietmann S, Paramor M, Niwa H, Smith A (2014) Genetic exploration of the exit from self-
1346 renewal using haploid embryonic stem cells. *Cell Stem Cell* 14: 385-393
1347
1348 Licatalosi DD, Yano M, Fak JJ, Mele A, Grabinski SE, Zhang C, Darnell RB (2012) Ptbp2 represses
1349 adult-specific splicing to regulate the generation of neuronal precursors in the embryonic brain. *Genes &*
1350 *Development* 26: 1626-1642
1351
1352 Lin H, Spradling AC (1997) A novel group of pumilio mutations affects the asymmetric division of
1353 germline stem cells in the Drosophila ovary. *Development* 124: 2463-2476
1354
1355 Liu GY, Sabatini DM (2020) mTOR at the nexus of nutrition, growth, ageing and disease. *Nature*
1356 *Reviews Molecular Cell Biology* 21: 183-203
1357
1358 Love MI, Huber W, Anders S (2014) Moderated estimation of fold change and dispersion for RNA-seq
1359 data with DESeq2. *Genome Biology* 15: 550
1360
1361 Lukong KE, Chang KW, Khandjian EW, Richard S (2008) RNA-binding proteins in human genetic
1362 disease. *Trends in Genetics:* 24: 416-425
1363
1364 Mandelboum S, Manber Z, Elroy-Stein O, Elkon R (2019) Recurrent functional misinterpretation of
1365 RNA-seq data caused by sample-specific gene length bias. *PLoS Biol* 17: e3000481
1366
1367 Mauger O, Lemoine F, Scheiffele P (2016) Targeted intron retention and excision for rapid gene
1368 regulation in response to neuronal activity. *Neuron* 92: 1266-1278
1369

1370 Maurin T, Lebrigand K, Castagnola S, Paquet A, Jarjat M, Popa A, Grossi M, Rage F, Bardoni B (2018)
1371 HITS-CLIP in various brain areas reveals new targets and new modalities of RNA binding by fragile X
1372 mental retardation protein. *Nucleic Acids Research* 46: 6344-6355
1373
1374 McCabe MP, Cullen ER, Barrows CM, Shore AN, Tooke KI, Laprade KA, Stafford JM, Weston MC
1375 (2020) Genetic inactivation of mTORC1 or mTORC2 in neurons reveals distinct functions in
1376 glutamatergic synaptic transmission. *Elife* 9: e51440.
1377
1378 Menon KP, Sanyal S, Habara Y, Sanchez R, Wharton RP, Ramaswami M, Zinn K (2004) The
1379 translational repressor Pumilio regulates presynaptic morphology and controls postsynaptic accumulation
1380 of translation factor eIF-4E. *Neuron* 44: 663-676

1381 Miles WO, Tschop K, Herr A, Ji JY, Dyson NJ (2012) Pumilio facilitates miRNA regulation of the E2F3
1382 oncogene. *Genes & Development* 26: 356-368
1383
1384 Miller MA, Olivas WM (2011) Roles of Puf proteins in mRNA degradation and translation. *Wiley*
1385 *Interdisciplinary Reviews RNA* 2: 471-492
1386
1387 Muraro NI, Weston AJ, Gerber AP, Luschnig S, Moffat KG, Baines RA (2008) Pumilio binds para
1388 mRNA and requires Nanos and Brat to regulate sodium current in Drosophila motoneurons. *The Journal*
1389 *of Neuroscience* 28: 2099-2109
1390
1391 Orr HT, Zoghbi HY (2007) Trinucleotide repeat disorders. *Annual review of neuroscience* 30: 575-621
1392 Otasek D, Morris JH, Boucas J, Pico AR, Demchak B (2019) Cytoscape Automation: empowering
1393 workflow-based network analysis. *Genome Biology* 20: 185
1394
1395 Pfaffl MW (2001) A new mathematical model for relative quantification in real-time RT-PCR. *Nucleic*
1396 *Acids Research* 29: e45
1397
1398 Preitner N, Quan J, Nowakowski DW, Hancock ML, Shi J, Tcherkezian J, Young-Pearse TL, Flanagan
1399 JG (2014) APC is an RNA-binding protein, and its interactome provides a link to neural development and
1400 microtubule assembly. *Cell* 158: 368-382
1401
1402 Qiu C, Dutcher RC, Porter DF, Arava Y, Wickens M, Hall TMT (2019) Distinct RNA-binding modules
1403 in a single PUF protein cooperate to determine RNA specificity. *Nucleic Acids Research* 47: 8770-8784
1404
1405 Raudvere U, Kolberg L, Kuzmin I, Arak T, Adler P, Peterson H, Vilo J (2019) g:Profiler: a web server for
1406 functional enrichment analysis and conversions of gene lists (2019 update). *Nucleic Acids Research* 47:
1407 W191-W198
1408
1409 Ravanidis S, Kattan FG, Doxakis E (2018) Unraveling the pathways to neuronal homeostasis and disease:
1410 mechanistic insights into the role of RNA-binding proteins and associated factors. *Int J Mol Sci* 19: 2280.
1411
1412 Rousseaux MWC, Tschumperlin T, Lu HC, Lackey EP, Bondar VV, Wan YW, Tan Q, Adamski CJ,
1413 Friedrich J, Twaroski K *et al* (2018) ATXN1-CIC Complex is the primary driver of cerebellar pathology
1414 in spinocerebellar ataxia type 1 through a gain-of-function mechanism. *Neuron* 97: 1235-1243 e1235
1415

1416 Rovelet-Lecrux A, Hannequin D, Raux G, Le Meur N, Laquerriere A, Vital A, Dumanchin C, Feuillette
1417 S, Brice A, Vercelletto M *et al* (2006) APP locus duplication causes autosomal dominant early-onset
1418 Alzheimer disease with cerebral amyloid angiopathy. *Nature Genetics* 38: 24-26
1419
1420 Salcedo-Arellano MJ, Dufour B, McLennan Y, Martinez-Cerdeno V, Hagerman R (2020) Fragile X
1421 syndrome and associated disorders: clinical aspects and pathology. *Neurobiology of Disease* 136: 104740
1422
1423 Sandweiss AJ, Brandt VL, Zoghbi HY (2020) Advances in understanding of Rett syndrome and MECP2
1424 duplication syndrome: prospects for future therapies. *Lancet Neurol* 19: 689-698
1425
1426 Shah S, Molinaro G, Liu B, Wang R, Huber KM, Ritcher JD (2020) FMRP control of ribosome
1427 translocation promotes chromatin modifications and alternative splicing of neuronal genes linked to
1428 autism. *Cell Reports* 30: 4459-4472
1429
1430 Shevchenko A, Tomas H, Havlis J, Olsen JV, Mann M (2006) In-gel digestion for mass spectrometric
1431 characterization of proteins and proteomes. *Nature Protocols* 1: 2856-2860
1432
1433 Singh K, Gaur P, Prasad S (2007) Fragile x mental retardation (Fmr-1) gene expression is down regulated
1434 in brain of mice during aging. *Mol Biol Rep* 34: 173-181
1435
1436 Singh K, Prasad S (2008) Differential expression of Fmr-1 mRNA and FMRP in female mice brain
1437 during aging. *Mol Biol Rep* 35: 677-684
1438
1439 Sivakumar S, Gorbsky GJ (2015) Spatiotemporal regulation of the anaphase-promoting complex in
1440 mitosis. *Nature Reviews Molecular Cell Biology* 16: 82-94
1441
1442 Smidak R, Sialana FJ, Kristofova M, Stojanovic T, Rajcic D, Malikovic J, Feyissa DD, Korz V, Hoeger
1443 H, Wackerlig J *et al* (2017) Reduced levels of the synaptic functional regulator FMRP in dentate gyrus of
1444 the Aging Sprague-Dawley rat. *Front Aging Neurosci* 9: 384
1445
1446 Subramanian A, Tamayo P, Mootha VK, Mukherjee S, Ebert BL, Gillette MA, Paulovich A, Pomeroy
1447 SL, Golub TR, Lander ES *et al* (2005) Gene set enrichment analysis: a knowledge-based approach for
1448 interpreting genome-wide expression profiles. *PNAS* 102: 15545-15550
1449
1450 Takeguchi R, Takahashi S, Kuroda M, Tanaka R, Suzuki N, Tomonoh Y, Ihara Y, Sugiyama N, Itoh M
1451 (2020) MeCP2_e2 partially compensates for lack of MeCP2_e1: a male case of Rett syndrome. *Mol*
1452 *Genet Genomic Med* 8: e1088
1453
1454 Tan Q, Zoghbi HY (2019) Mouse models as a tool for discovering new neurological diseases. *Neurobiol*
1455 *Learn Mem* 165: 106902
1456
1457 Temme C, Simonelig M, Wahle E (2014) Deadenylation of mRNA by the CCR4-NOT complex in
1458 Drosophila: molecular and developmental aspects. *Front Genet* 5: 143
1459
1460 Tereshchenko A, Magnotta V, Epping E, Mathews K, Espe-Pfeifer P, Martin E, Dawson J, Duan W,
1461 Nopoulos P (2019) Brain structure in juvenile-onset Huntington disease. *Neurology* 92: e1939-e1947
1462
1463 Thul PJ, Akesson L, Wiking M, Mahdessian D, Geladaki A, Ait Blal H, Alm T, Asplund A, Bjork L,
1464 Breckels LM *et al* (2017) A subcellular map of the human proteome. *Science* 356

1465
1466 Tyanova S, Temu T, Sinitcyn P, Carlson A, Hein MY, Geiger T, Mann M, Cox J (2016) The Perseus
1467 computational platform for comprehensive analysis of (prote)omics data. *Nat Methods* 13: 731-740
1468
1469 Untergasser A, Cutcutache I, Koressaar T, Ye J, Faircloth BC, Remm M, Rozen SG (2012) Primer3--new
1470 capabilities and interfaces. *Nucleic Acids Research* 40: e115
1471
1472 Uyhazi KE, Yang Y, Liu N, Qi H, Huang XA, Mak W, Weatherbee SD, de Prisco N, Gennarino VA,
1473 Song X *et al* (2020) Pumilio proteins utilize distinct regulatory mechanisms to achieve complementary
1474 functions required for pluripotency and embryogenesis. *PNAS* 7:7851-7862.
1475
1476 Van Etten J, Schagat TL, Hrit J, Weidmann CA, Brumbaugh J, Coon JJ, Goldstrohm AC (2012) Human
1477 Pumilio proteins recruit multiple deadenylases to efficiently repress messenger RNAs. *The Journal of*
1478 *Biological Chemistry* 287: 36370-36383
1479
1480 Vandesompele J, De Preter K, Pattyn F, Poppe B, Van Roy N, De Paepe A, Speleman F (2002) Accurate
1481 normalization of real-time quantitative RT-PCR data by geometric averaging of multiple internal control
1482 genes. *Genome Biology* 3(7): RESEARCH0034
1483
1484 Wamsley B, Jaglin XH, Favuzzi E, Quattrocolo G, Nigro MJ, Yusuf N, Khodadadi-Jamayran A, Rudy B,
1485 Fishell G (2018) Rbfox1 mediates cell-type-specific splicing in cortical interneurons. *Neuron* 100: 846-
1486 859 e847
1487
1488 Wang X, Zamore PD, Hall TM (2001) Crystal structure of a Pumilio homology domain. *Molecular Cell*
1489 7: 855-865
1490
1491 Weidmann CA, Raynard NA, Blewett NH, Van Etten J, Goldstrohm AC (2014) The RNA binding
1492 domain of Pumilio antagonizes poly-adenosine binding protein and accelerates deadenylation. *RNA* 20:
1493 1298-1319
1494
1495 Weyn-Vanhentenryck SM, Mele A, Yan Q, Sun S, Farny N, Zhang Z, Xue C, Herre M, Silver PA, Zhang
1496 MQ *et al* (2014) HITS-CLIP and integrative modeling define the Rbfox splicing-regulatory network
1497 linked to brain development and autism. *Cell Reports* 6: 1139-1152
1498
1499 Zamore PD, Bartel DP, Lehmann R, Williamson JR (1999) The PUMILIO-RNA interaction: a single
1500 RNA-binding domain monomer recognizes a bipartite target sequence. *Biochemistry* 38: 596-604
1501
1502 Zamore PD, Williamson JR, Lehmann R (1997) The Pumilio protein binds RNA through a conserved
1503 domain that defines a new class of RNA-binding proteins. *RNA* 3: 1421-1433
1504
1505 Zhang C, Frias MA, Mele A, Ruggiu M, Eom T, Marney CB, Wang H, Licatalosi DD, Fak JJ, Darnell RB
1506 (2010) Integrative modeling defines the Nova splicing-regulatory network and its combinatorial controls.
1507 *Science* 329: 439-443
1508
1509 Zhang M, Chen D, Xia J, Han W, Cui X, Neuenkirchen N, Hermes G, Sestan N, Lin H (2017) Post-
1510 transcriptional regulation of mouse neurogenesis by Pumilio proteins. *Genes & Development* 31: 1354-
1511 1369
1512

1513 Zoghbi HY, Bear MF (2012) Synaptic dysfunction in neurodevelopmental disorders associated with
1514 autism and intellectual disabilities. *Cold Spring Harb Perspect Biol* 4: a009886
1515
1516 Zylka MJ, Simon JM, Philpot BD (2015) Gene length matters in neurons. *Neuron* 86: 353-355

1517

Figure 1, Botta et al.

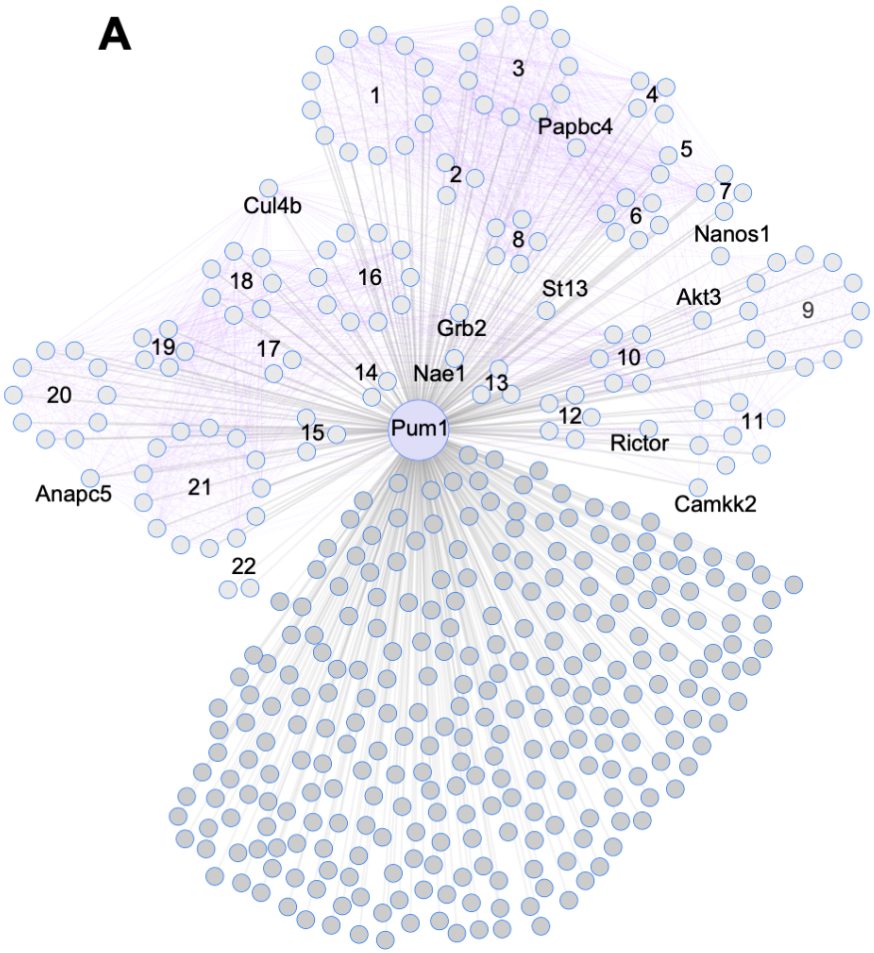

Cluster 1
Acin1
Ddx3x
Dhx15
Eftud2
Hnrnpul1
Rbm39
Sf3b3
Snrnp200
Srrt
Usp46
Wdr20
Wdr48

Cluster 2
Aff4
Mllt1
Mllt3

Cluster 3
Ctif
Eif2s1
Eif2s2
Eif2s3x
Eif2s3y
Eif3b
Eif3f
Eif3l
Eif4a3
Eif4g3
Eif5

Cluster 4
Elavl4
Etf1
Upf1
Thrap3

Cluster 5
Hnrnpa0
Hnrnpl

Cluster 6
D1Pas1
Khdrbs1
Snd1
Ssb
Ssbp2
Ssbp3

Cluster 7
Csde1
Paip1
Rae1
Rangap1

Cluster 8
Ago2
Cnot1
Fmrp
Pum2
Rbfox3

Cluster 9
Atg7
Brsk2
Fga
Fgb
Fgg
Madd
Pck2
Pex5l
Rab11fip5
Snx2
Snx4
Stxbp5l

Cluster 10
Matr3
Pfkfb2
Pfkl
Pfkm
Pfkp
Pspc1

Cluster 11
Cad
Lppr4
Lrpprc
Pten
Rptor
Tsc1
Tsc2

Cluster 12
Camk1d
Clasp1
Clip2
Rhob
Rhot1

Cluster 13
Prmt5
Rpl24
Tuba1a

Cluster 14
Kcna1
Kcna2

Cluster 15
Actbl2
Actl6b
Smarce1

Cluster 16
Cul1
Cul4a
Mycbp2
Pja1
Rlim
Rnf14
Trim32
Uba3
Uba5

Cluster 17
Pi4ka
Ttc7b

Cluster 18
Eea1
Elp3
Papss1
Pikr4
Prpsap2
Ruvbl1
Zyg11b

Cluster 19
Hdac2
Kdm1a
Ogt
Rbbp7
Zmym2

Cluster 20
Ppp1cb
Ppp1r12a
Ppp1r12b
Ppp1r12c
Ppp1r16b
Ppp1r21
Ppp2r5c
Ppp2r5d
Ppp6r1
Ppp6r2

Cluster 21
Anapc1
Anapc2
Anapc7
Anapc10
Cdc16
Cdc23
Cdc27
Cep97
Dnaja1
Fzr1
Sh3kbp1
Znf281

Cluster 22
Osbpl1
Osbpl8

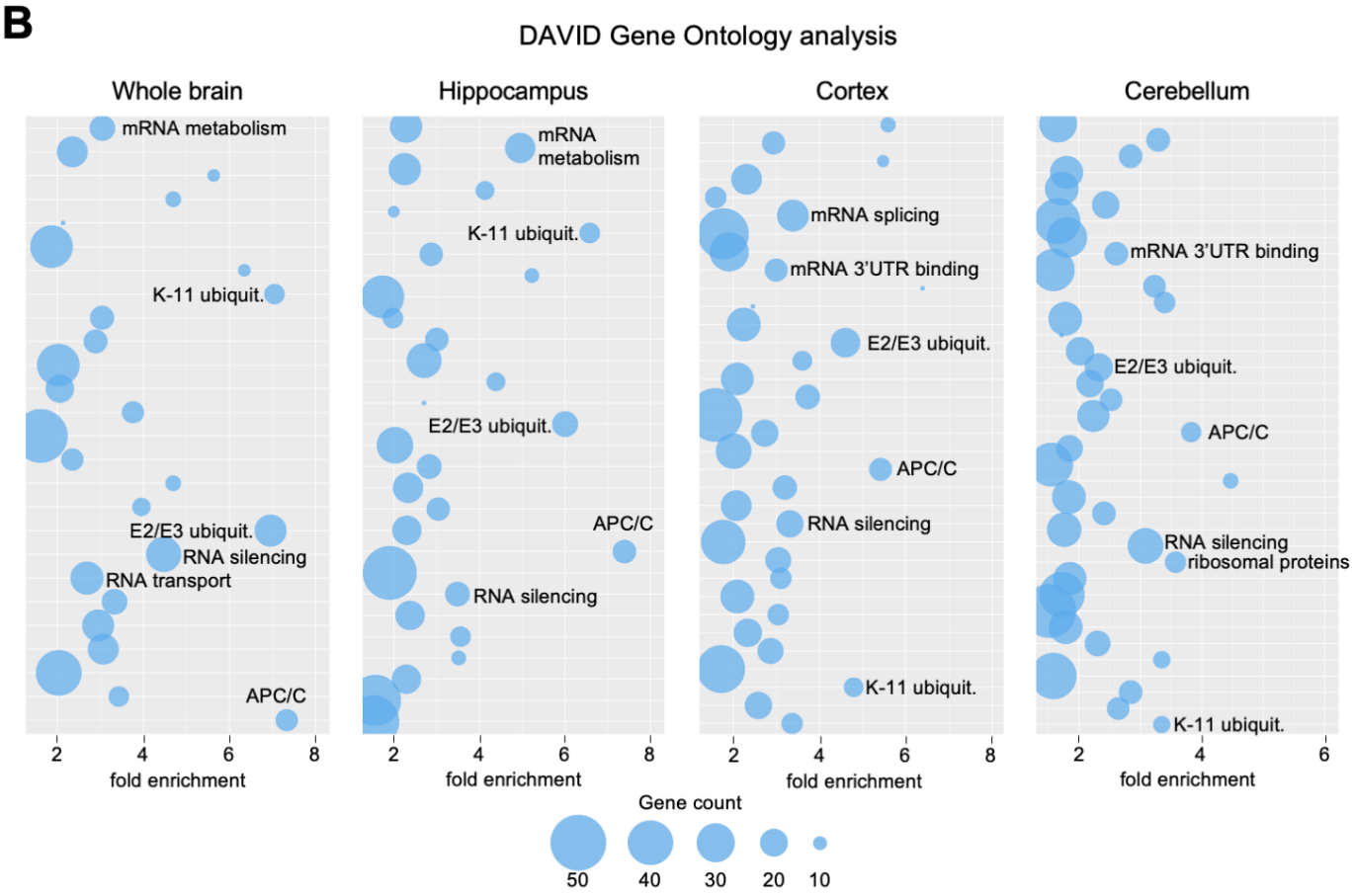

Figure 2. Botta et al.

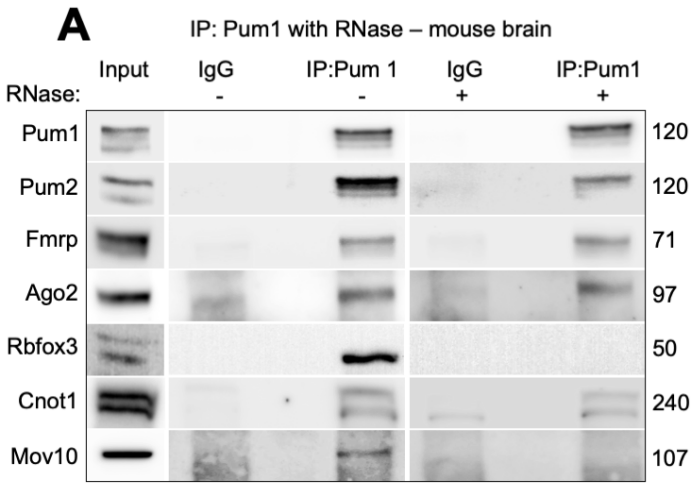

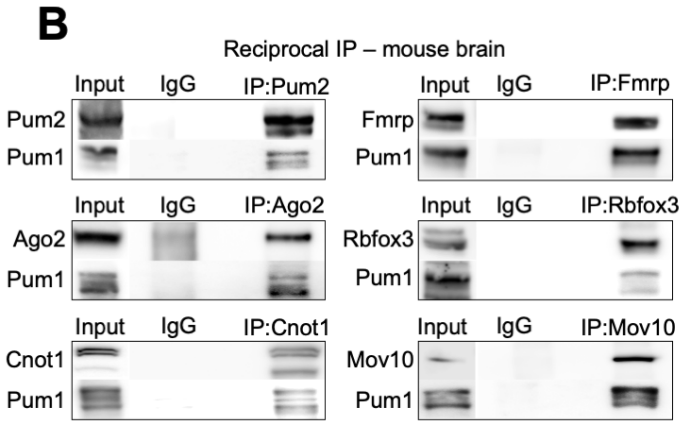

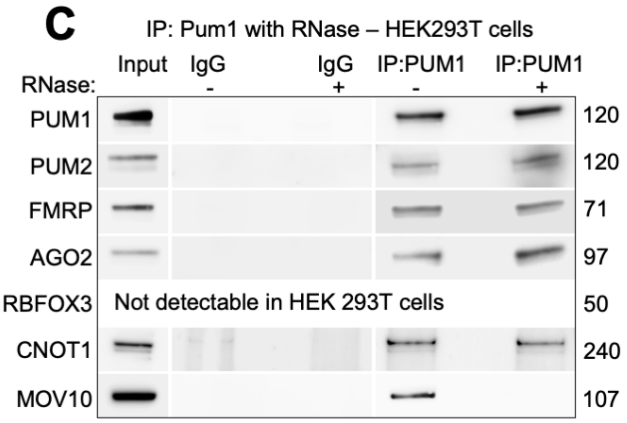

Figure 3. Botta et al.

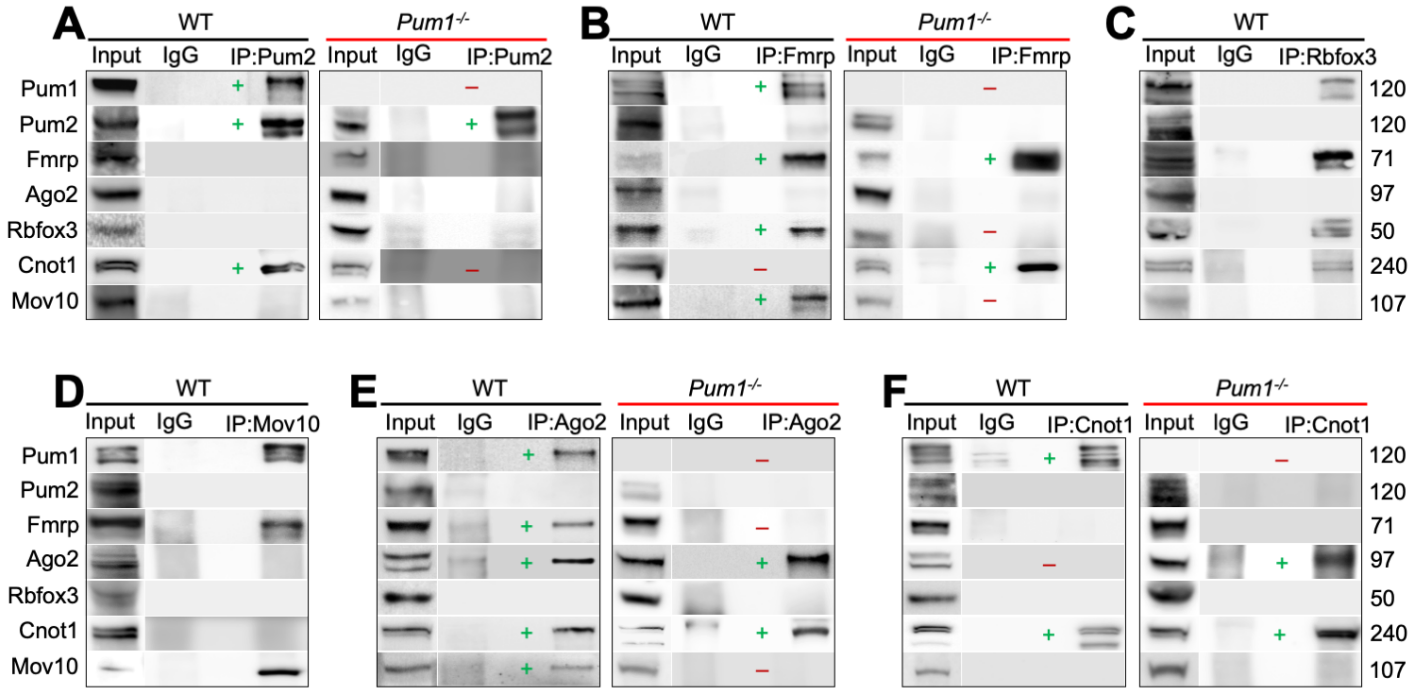

Figure 4. Botta et al.

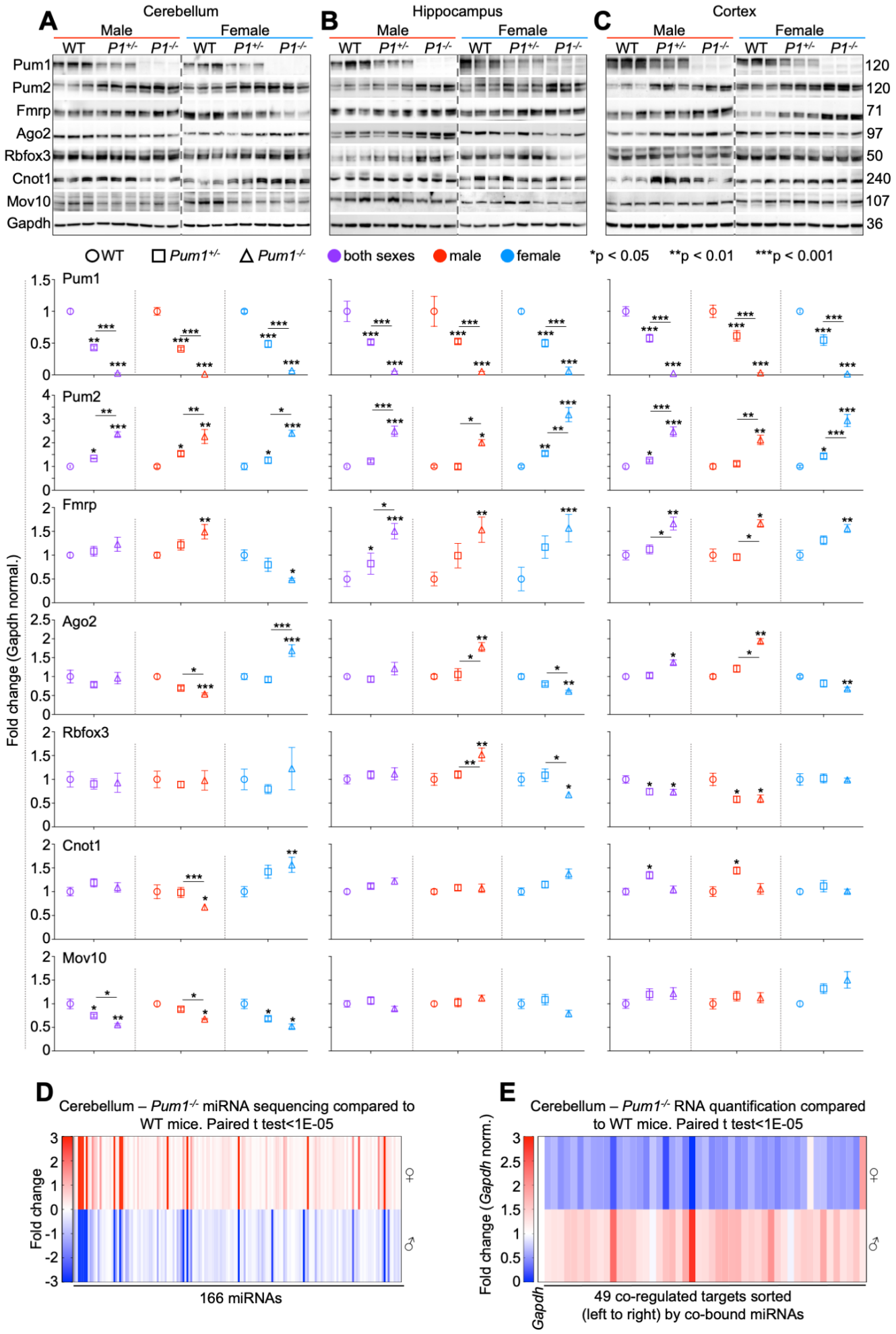

Figure 5. Botta et al.

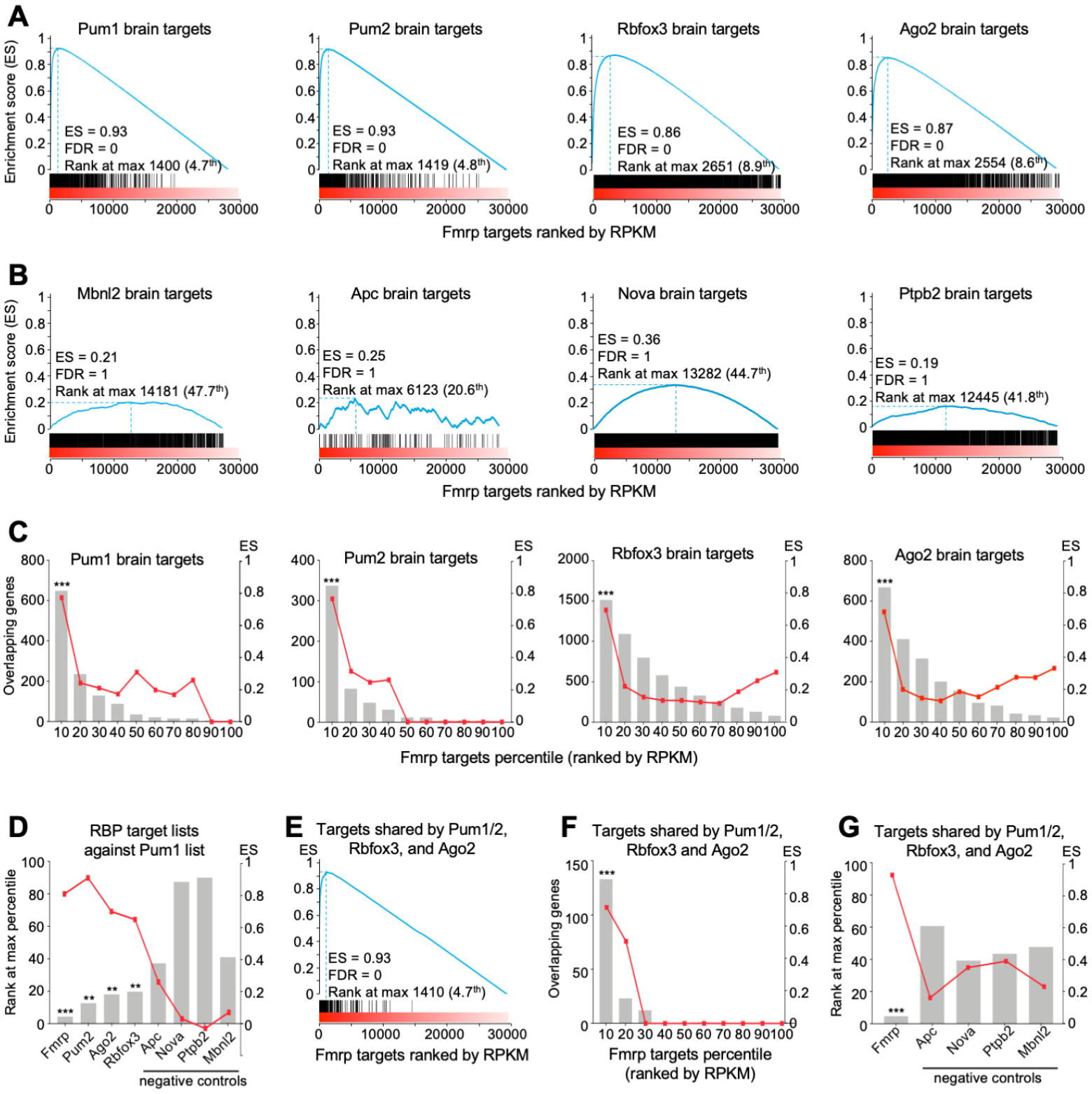

Figure 6. Botta et al.

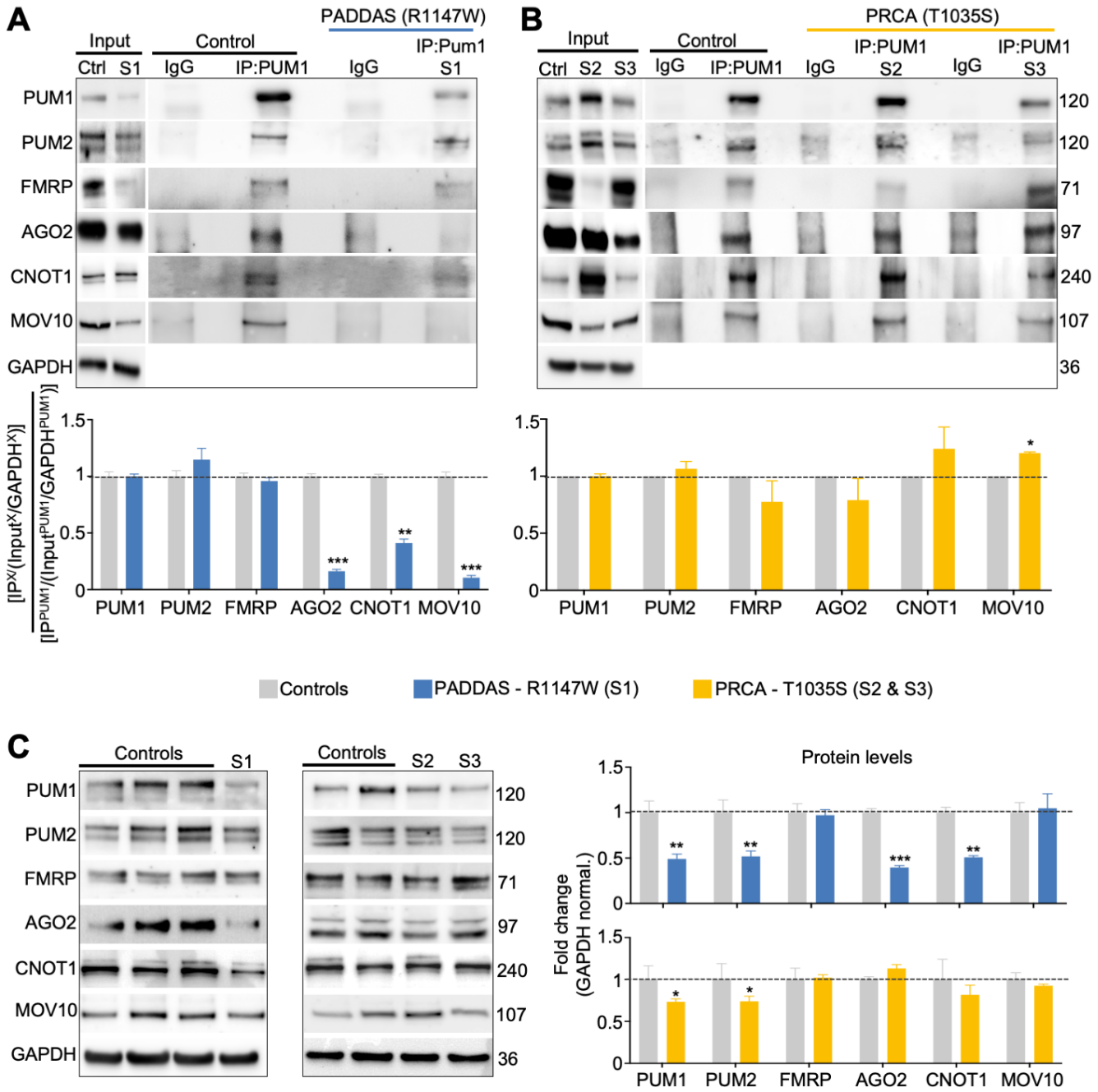

Figure 7. Botta et al.

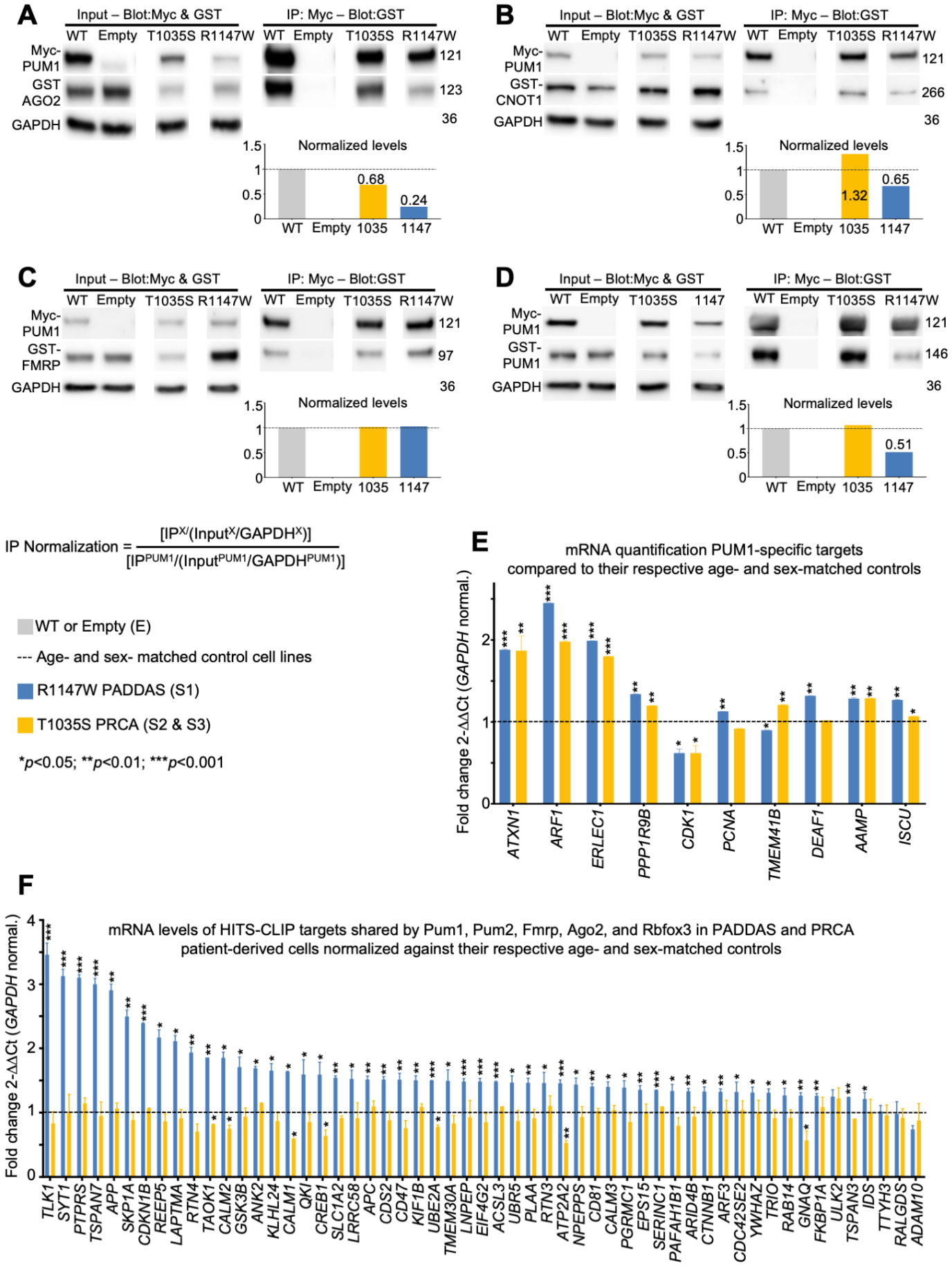

Figure 1–figure supplement 1. Botta et al.

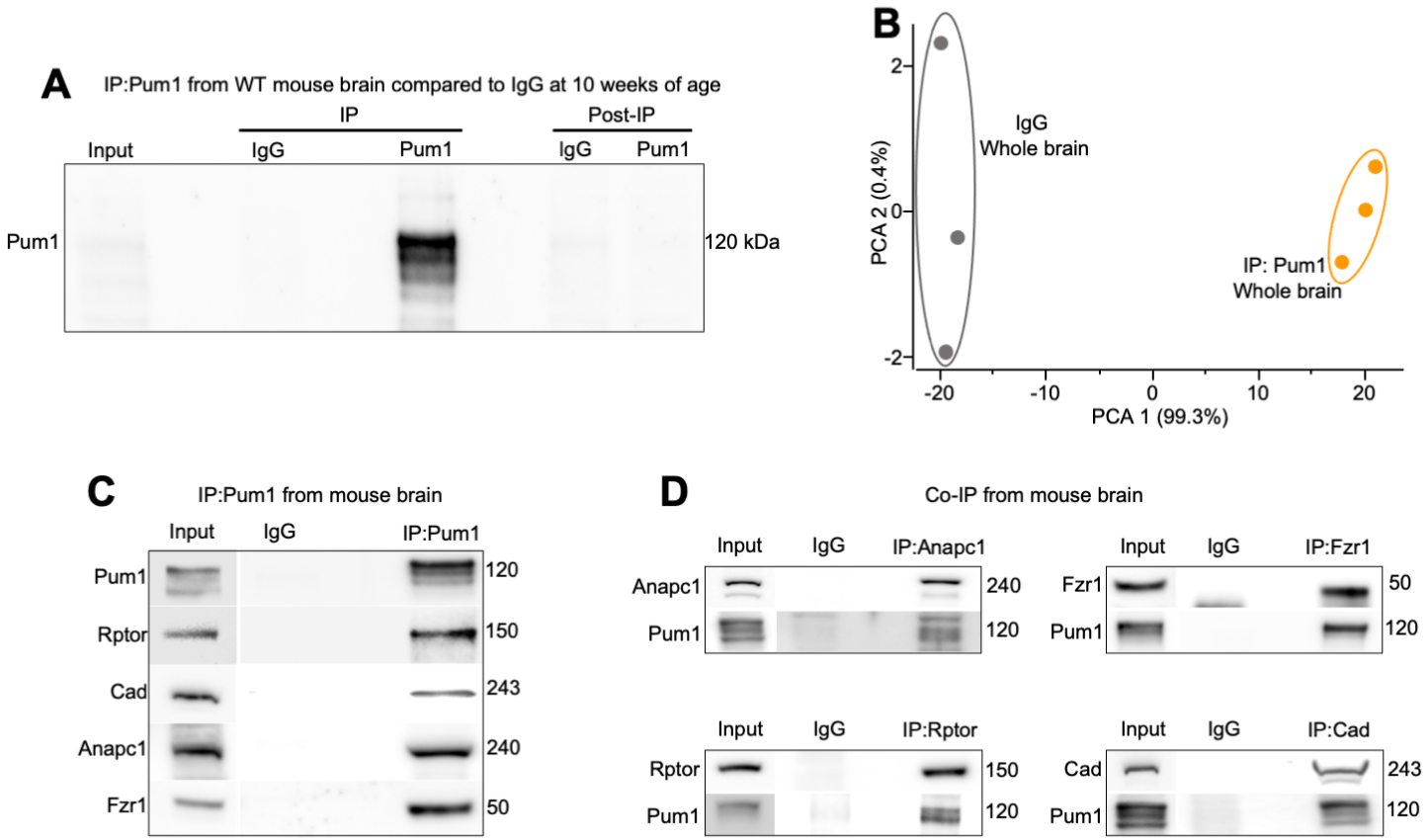

Figure 1–figure supplement 2. Botta et al.

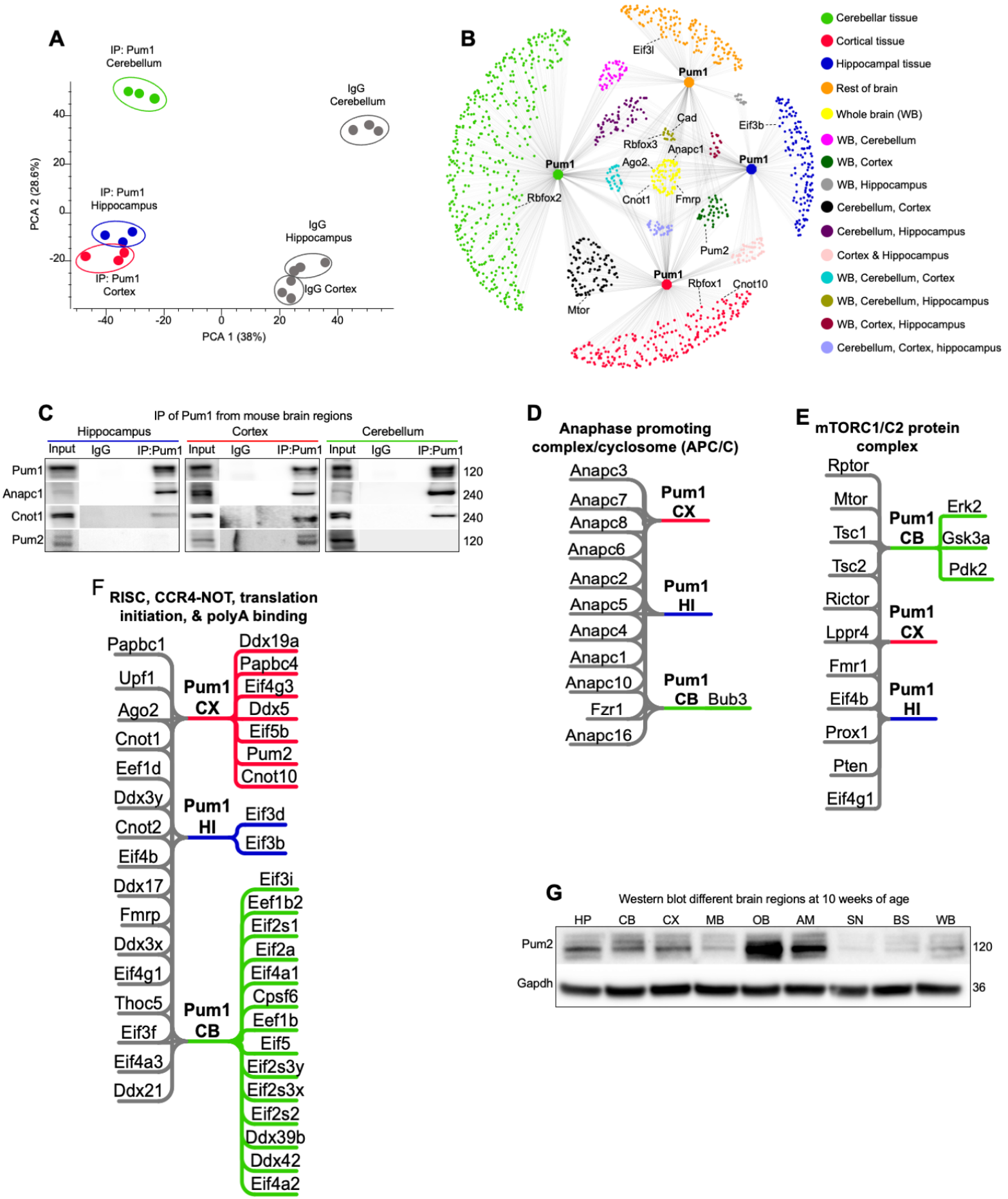

Figure 2–figure supplement 1. Botta et al.

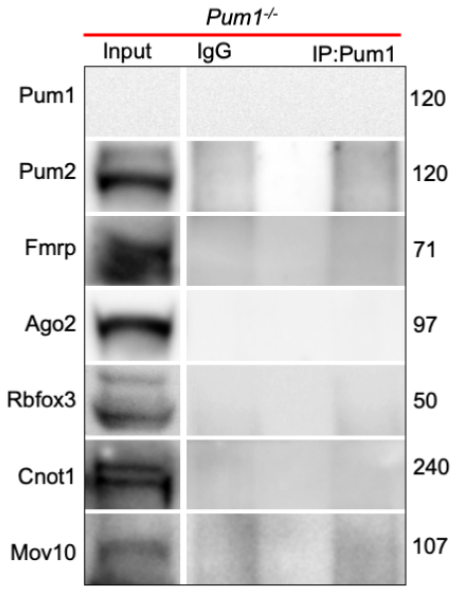

Figure 3–figure supplement 1. Botta et al.

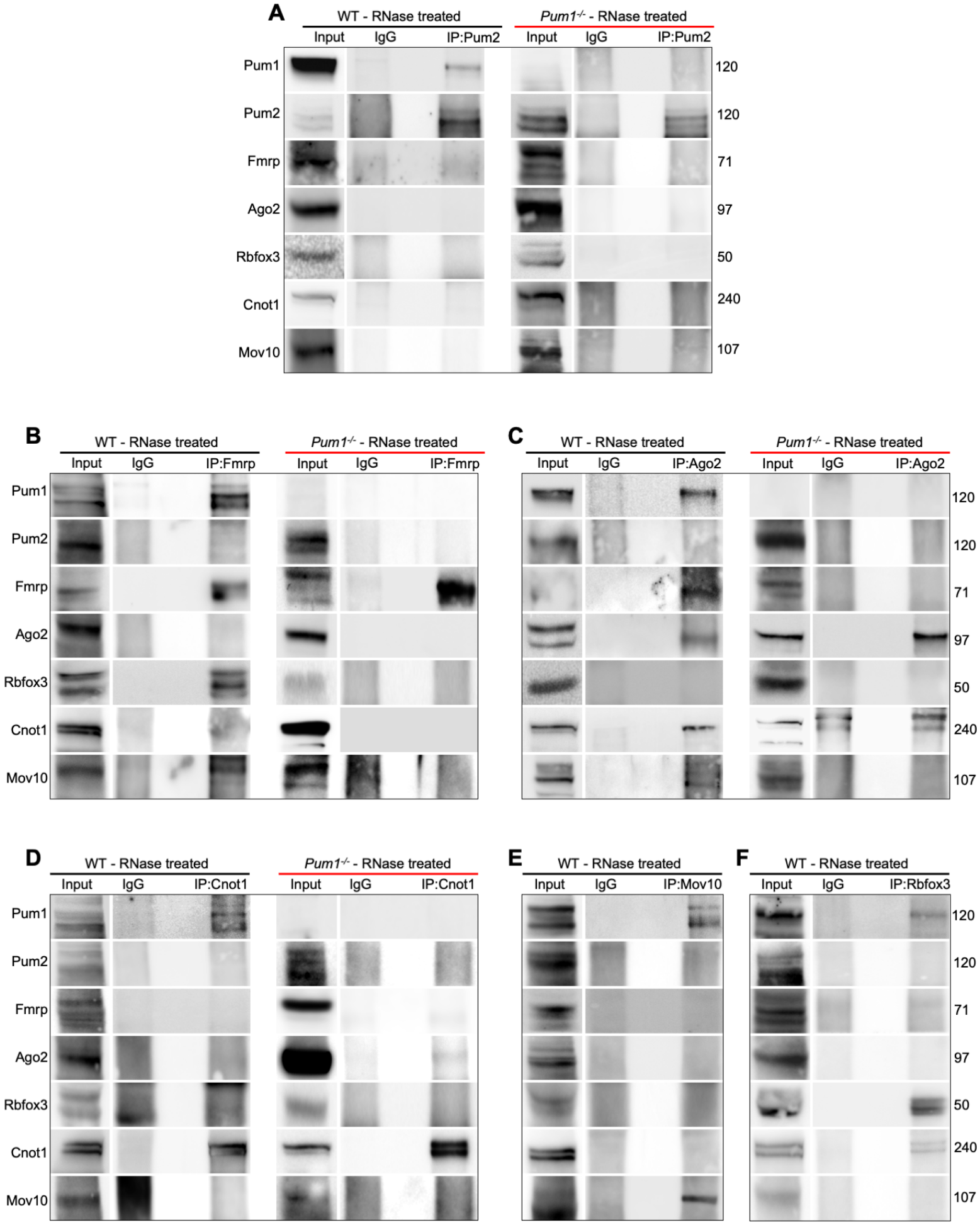

Figure 4–figure supplement 1. Botta et al.

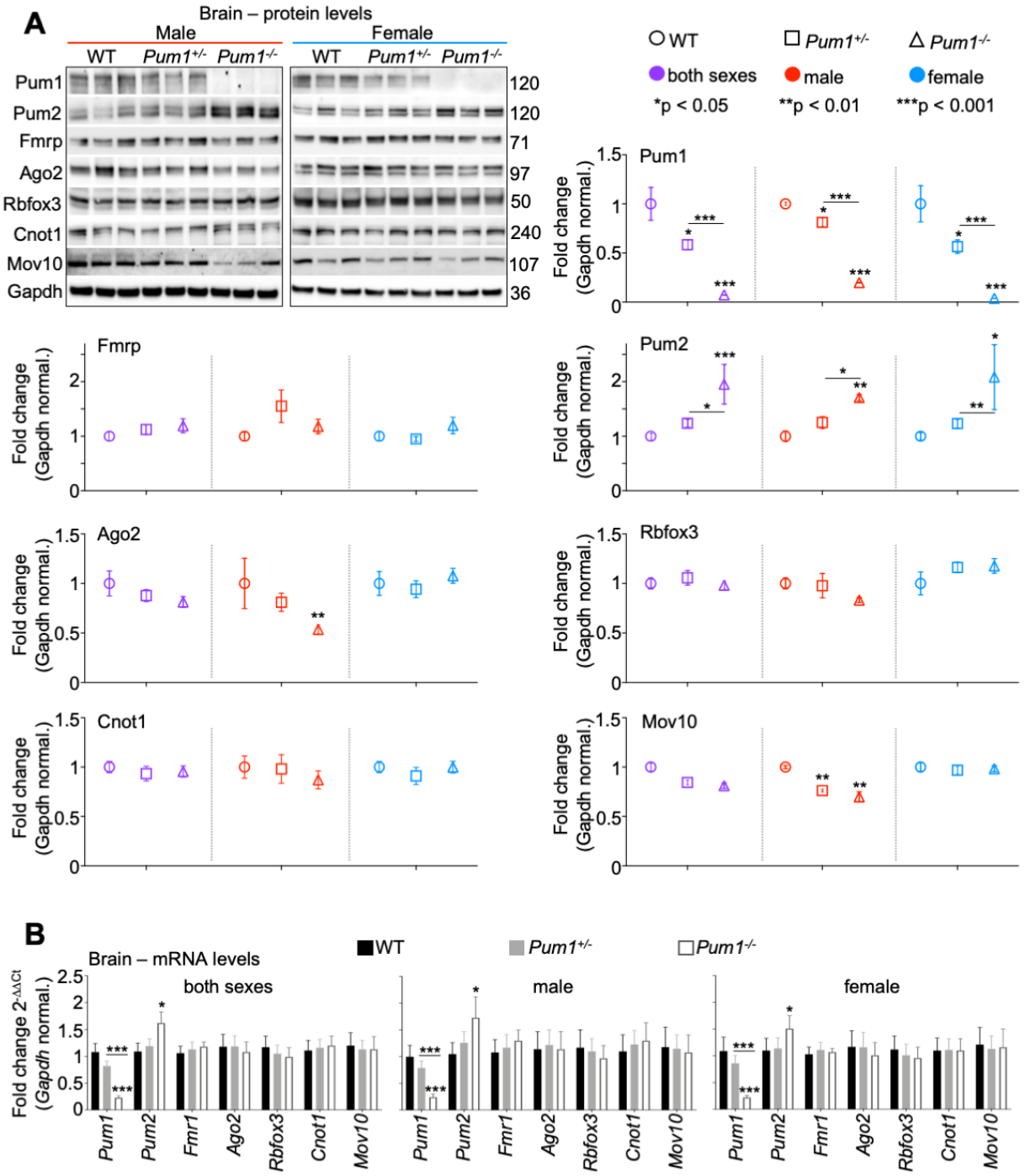

Fiigure 4–figure supplement 2. Botta et al.

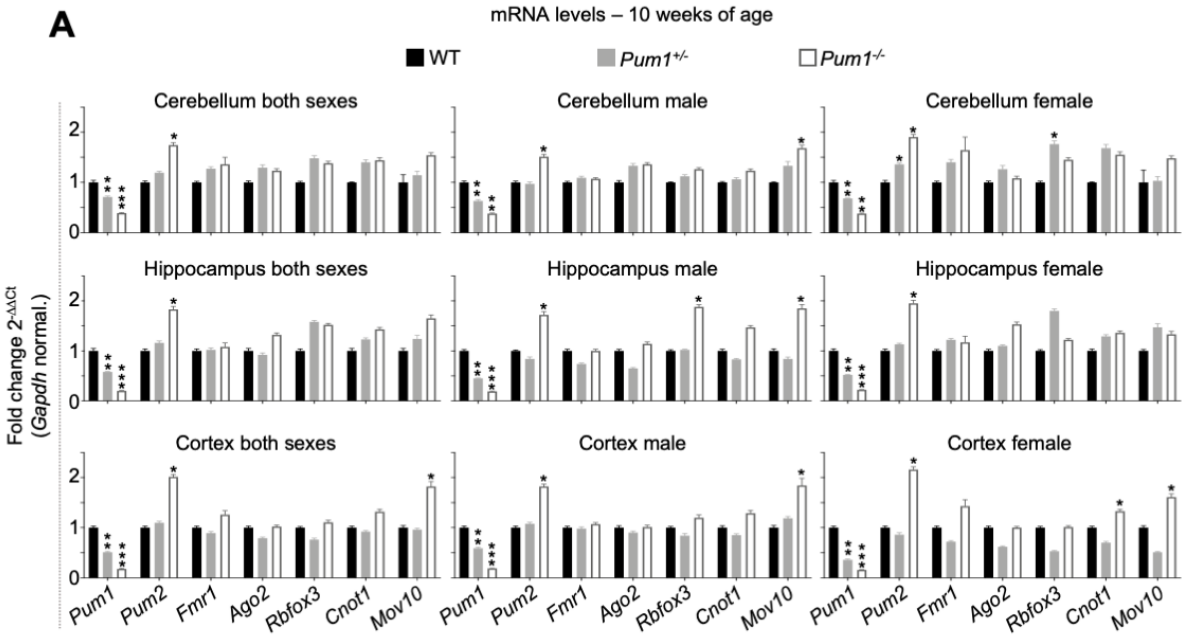

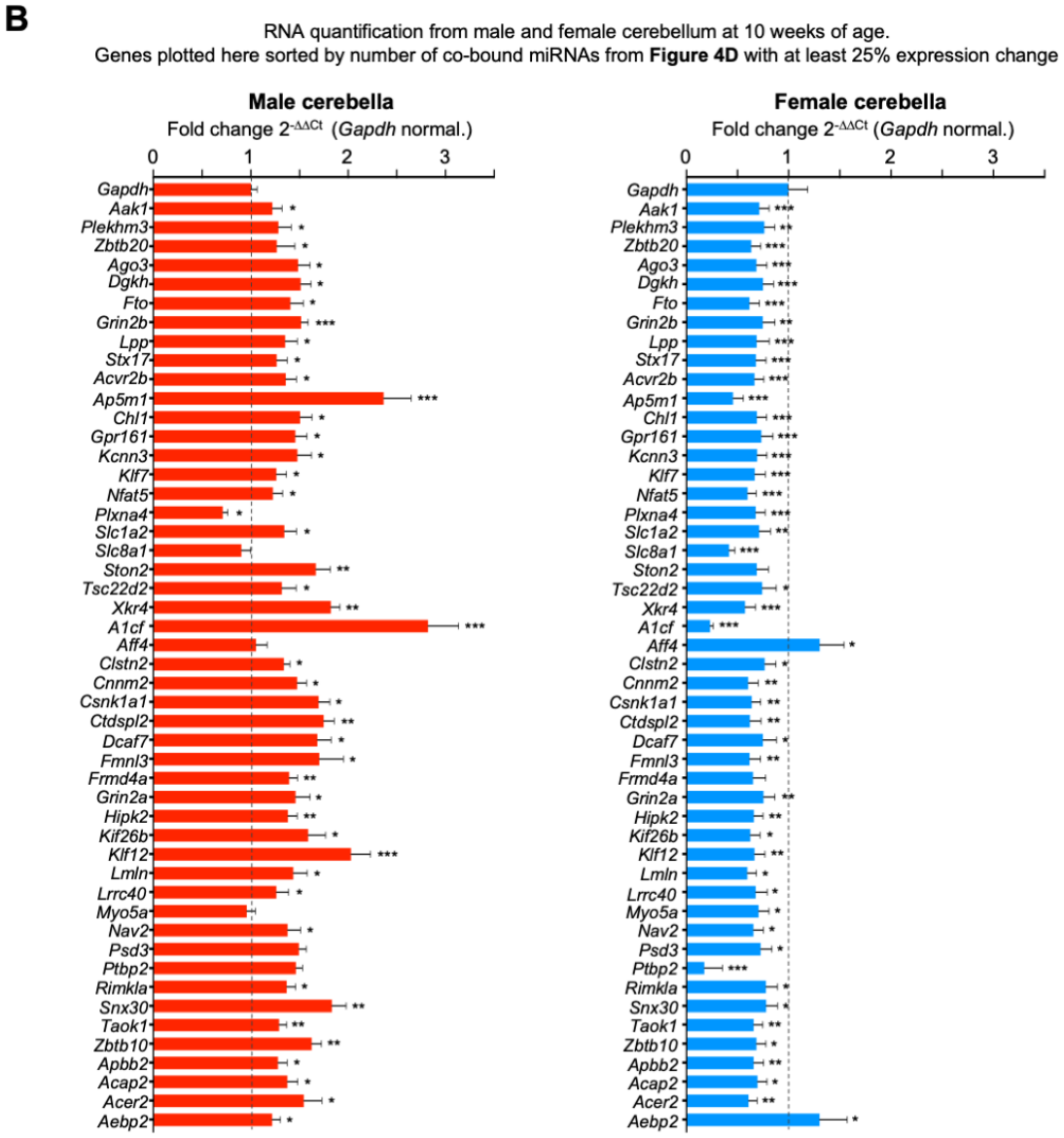

Figure 5–figure supplement 1. Botta et al.

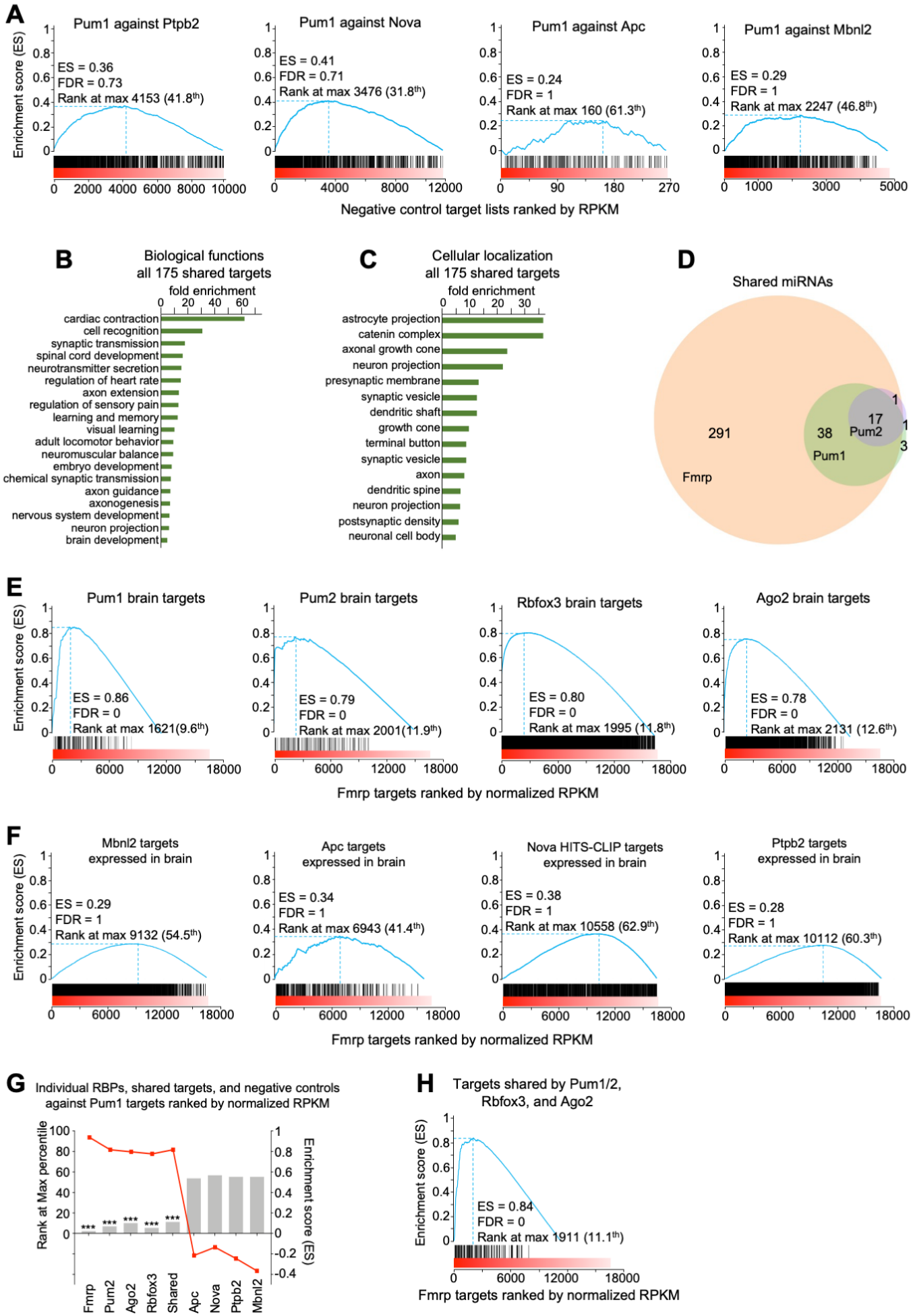

Figure 6–figure supplement 1. Botta et al.

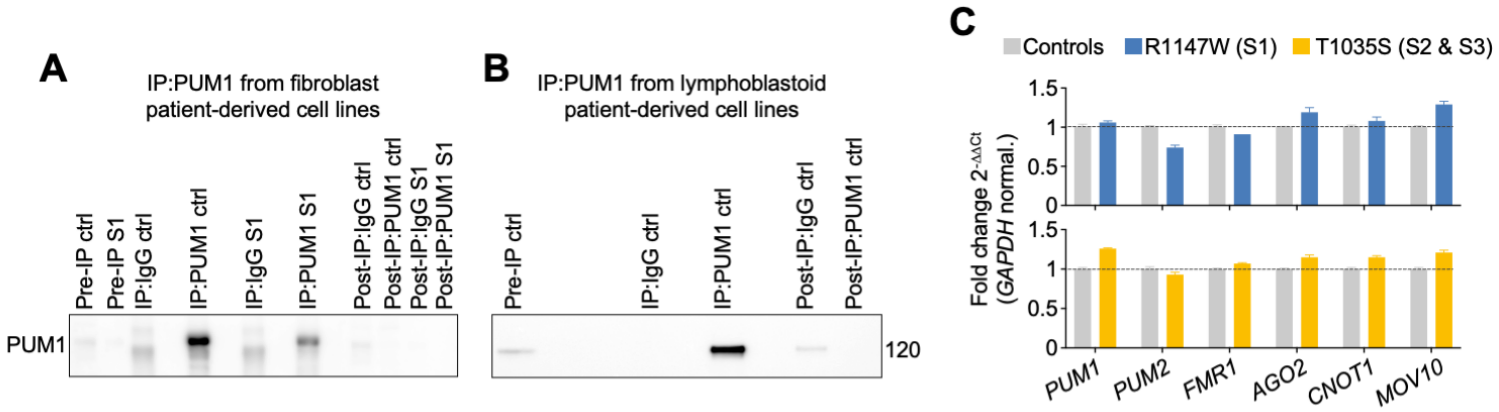
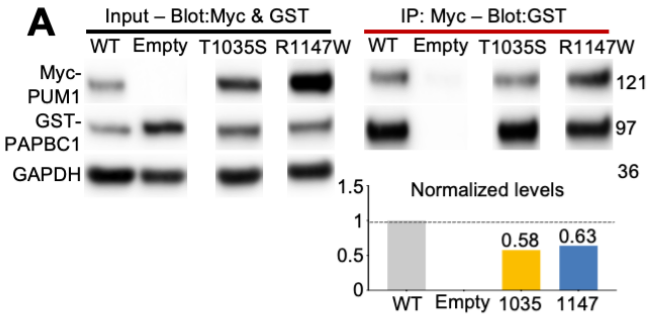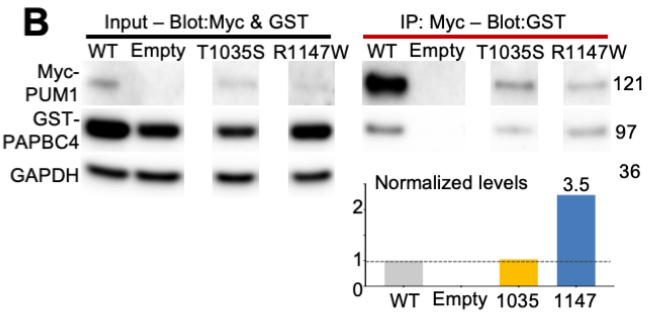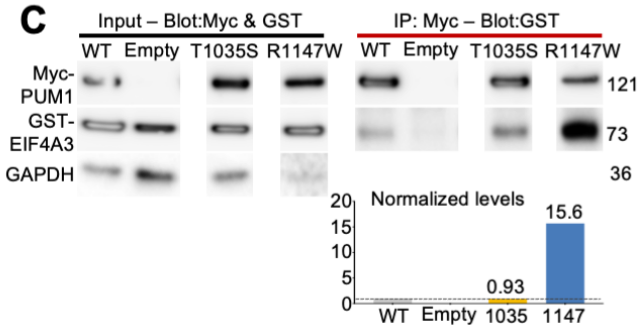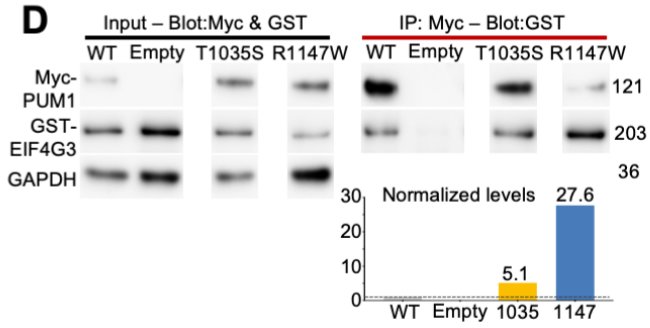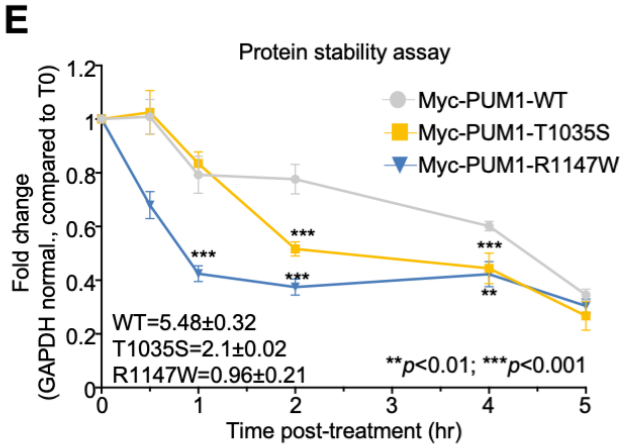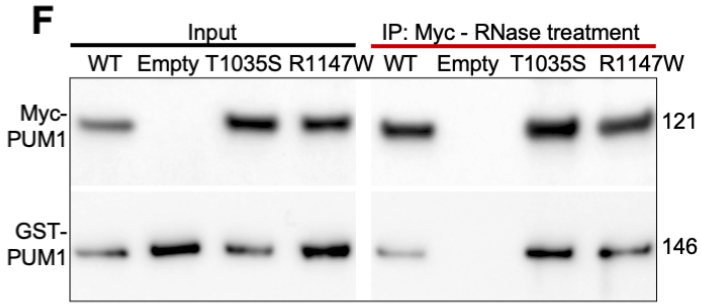
Figure 7–figure supplement 1. Botta et al.